Magnetic field-mappings in low field large-aperture accelerator magnets

Vetle Elvebakken Andersen

Abstract

A rotating coil measurement is one of the most common methods for measuring particle accelerator magnets, as it offers sufficient measurement precision and robustness. Nevertheless, the rotating coil method suffers from low flexibility, due to the need for higly specialized coils for each magnet-aperture.

This thesis proposes a solution to increase the flexibility and validates the field reconstruction from several measurements acquired in different positions inside the magnet aperture. The validation were carried out on a magnet with a low field and a large-aperture geometry, which normally would require the manufacturing of a specialized coil. Using the lower-order multipoles acquired on a circular trajectory with sufficient precision, and a measurement radius of 45 *mm* the reconstructed multipoles resulted in higher precision than for a single rotating coil measurement in the central position and a Single-Stretched Wire measurement taken with a measurement radius of 50 *mm*

Sammendrag

Roterende-spole målinger er en av de mest brukte metodene for målinger av partikkelakselerator-magneter, fordi den har høy nok presisjon og robusthet. En av begrensingene til målemetoden er at den gir lav fleksibilitet, da den avhenger av å ha spoler tilpasset forskjellige magneters apertur-geometri.

Denne oppgaven foreslår en metode for å øke fleksibiliteten og validerer felt-rekonstruksjonen til flere forskjellige målinger tatt i forskjellige posisjoner i magnetfeltet. Magneten som ble målt hadde et lavt magnetfelt kombinert med en stor radius, en kombinasjon som er svært vanskelig å måle med normale metoder. Ved å kun bruke lavere ordens multipoler målt med nok presisjon og en måleradius på $45mm$, er det mulig å rekonstrure de resterende multipolene med høyere presisjon enn presisjonen gitt fra en måling med roterende-spole tatt sentralt i magnetfeltet eller fra en måling med Single-Stretched Wire gjort med en radius på $50mm$.

Contents

Figures

Tables

Glossary

field harmonics See multipoles. 10

higher-order Multipoles above the order n=6 is for this thesis considered as higher-order. 48

holomorphic Let $\mathcal{D}$ be an open subset in the complex domain $\mathcal{C}$, then if a function **f** is complex-differentiable at every point of $\mathcal{D}$ its called holomorphic in the domain $\mathcal{D}$ [1]. It is the complex equivalent of an analytic function . 10

multipoles Magnetic multipoles, also known as field harmonics, a set of Fourier coefficients used to describe the field quality in accelerator magnets. xv, 10

singular A singular matrix is a matrix where the determinant is 0. Furthermore, such a matrix has no inverse . 16

units A multipole scaled accordingly to $\frac{C_n}{B_1} \cdot 1e^4$, meaning it is normalized to the main field normal component. 11, 38

Nomenclature

Throughout the thesis the following nomeclature has been adopted. It is presented here with the respective units given in brackets

$\mathbf{B}$: Magnetic Flux Density - [T]

Φ: Magnetic Flux - [$\frac{T}{m^2}$]

r_0: Reference Radius of a Magnetic Measurement - [m]

r_c: Measurement radius of the small coil - [m]

n: Variable used to indicate order for different other variables - [Integer]

B_n/A_n: Normal/Skew Magnetic Multipole Component of Order n- [T]

b_n/a_n: Normal/Skew Magnetic Multipole Component normalized to the main field component of order n - [$\frac{B_n}{B_1} \cdot 1e4$]

N: Highest multipole order used for the reconstruction with the oversampling method - [n]

K: Number of multipoles reconstructed on the reference radius - [n]

I: Number of measurement positions used for the reconstruction - [n]

C_n: Total multipole of order n, $C_n = B_n + iA_n$ - [T]

c_n: Total multipole of order n, $c_n = b_n + ia_n$ - [Units]

σ: The standard-deviation of an value. Given in the same unit as the main value.

Chapter 1

Introduction

Preface

This thesis concludes my three-year bachelor program at the Norwegian University of Science and Technology, where the last part was spent in CERN's technical student program. Here I was fortunate to work on the project I will present as my thesis.

I would like to thank my supervisor Dr. Ing Carlo Petrone, for all the help and guidance I have received on the project, as well as helpful advice that went deeper than just the technical problems I encountered. It truly was a wonderful year.

Thanks to Dr. Ing Melvin Liebsch for always being able to solve my technical problems like they were nothing, as well as the rest of the Magnetic Measurement section for being such a welcoming group.
I would like to express my gratitude to my professors at NTNU for encouraging the students to apply to CERN, and my supervisor at NTNU Prof. Ian Norheim for helpful guidance on my thesis.

1.1 Background

Conseil Européen pour la Recherche Nucléaire (CERN), is a European research organization focusing on high-energy particle physics. Established in 1953 close to Geneve as a joint effort from scientists in Europe after the Second World War, it has since grown to include 23 states as members and is one of the worlds leading research institutes. Since 1953 CERN has pushed the frontiers of physics many times, such as the discovery of the Higgs-boson [2] in 2012, or the rare electron decay [3] of the Pion particle, which was the first discovery (1957) of the first accelerator built at CERN. They operate the worlds largest particle accelerator, the Large Hadron Collider (LHC). The LCH is part of a complex of eight particle-accelerators, starting from energies at 4.2 MeV in Linear Accelerator 4 (LINAC 4), and then accelerating particles up to 6.5 TeV in the LHC[1], as illustrated by figure 1.1. The reason CERN is smashing particles

---

[1] https://home.cern/science/accelerators, visited March 2022
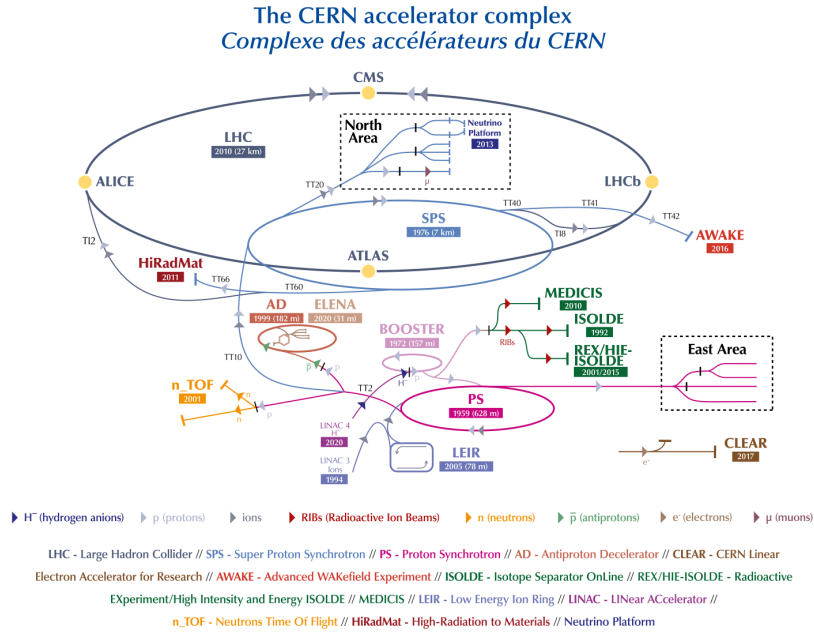
Figure 1.1: Overview of the CERN accelerator complex, showing the multitude of accelerators at CERN. The circular ones are illustrated by a circle. Taken from [4]

together at high speeds comes from Einsteins famous equation [5]:

$$E = mc^2 \qquad (1.1)$$

In the context of colliding particles, it states that the greater the speed the particles are accelerated, the heavier particles comes from the collision. These particles are the *raison d'être* for CERN's quest to understand the building blocks of matter and the universe's physical laws. Keeping the particles, which are traveling close to light speed, in their ideal orbit, and then focusing before crashing them together in a detector is no small task. To do this, magnets are used, and a precise knowledge of the magnetic fields is needed.

CERN's *Testing and Measurement* section, under the *Technology* department and the *Magnets, Superconductors, Testing, and Measurement* group is tasked with measuring the magnets used at CERN and doing Research and Development on methods for magnetic measurement. The magnets used at CERN range from superconducting magnets cooled up to 1.9 K used in the LHC, permanent magnets, and normal-conducting magnets used in other pre-accelerators injecting particles into LHC.

1.2 Project description

This thesis builds upon the theory laid out in the Ph.D. thesis "Combining rotating-coil measurements of large-aperture accelerator magnets" [6] by O. Koster, where it is shown that it is
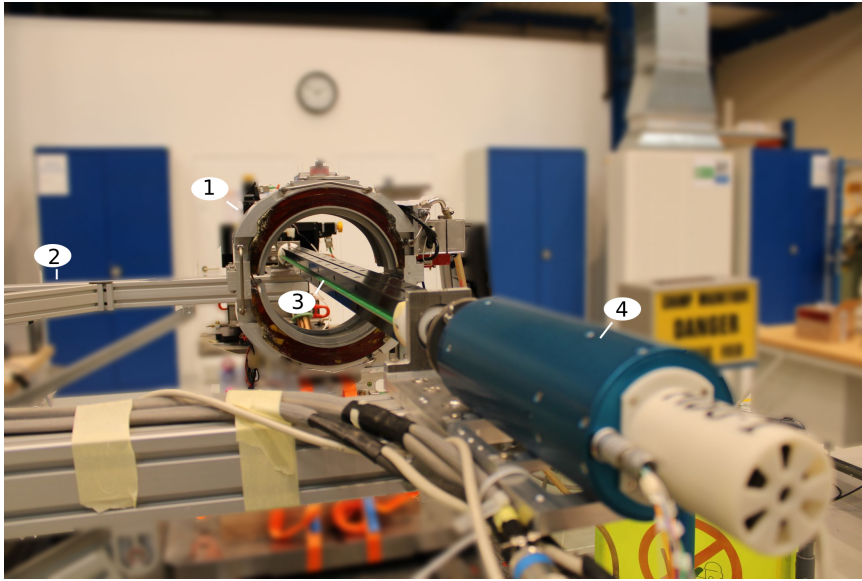
Figure 1.2: Picture of a magnetic measurement setup with the Rotating-Coil Mapper. Pictured is 1) the AirCoil magnet 2) linear stages 3) the coil and 4) the motor rotating the coil. The linear stages can be moved.

feasible to combine several rotating coil measurements to qualify a large-aperture magnet. At the time it was written, Koster found some challenges given the low precision in the positioning of the coil stages. However, it is feasible to do this type of measurement today due to more precise positioning systems.

With the making of the automatic Rotating-Coil Mapper (RCM), the thesis starts with a subsequent verification measurement on a magnet and compares the result with two other methods. The magnet chosen for the project has a large aperture and a very low field level which is the perfect combination to showcase the method's flexibility compared to the normal methods. Then, I will look into some guidelines for the method, such as which parameters have the most influx on the outcome.

Rotating Coil Mapper

A huge part of my project here at CERN has been developing the Rotating Coil Mapper, everything from coding the movement of the linear stages, and rotation of the coil, up to the translation of the mathematical algorithm into Python code which calculates the Least-Squares fit.
This thesis starts at the point where the Rotating-Coil Mapper is made, and the first measurements are carried out. Figure 1.2 shows the measurement setup with which the thesis starts. The theory presented in later chapters might be more easily grasped with a small illustration of the system in mind. In short, the idea is to rotate the coil and then move it to another place inside the magnet, rotate it again, and do this some number of times. Afterward, the measurements are combined into one common measurement.

1.2.1 Scope of the thesis

The scope of my thesis will be the theory and measurements relevant to measure a large-aperture magnet with the proposed oversampling method. I will not write in detail about all the hardware and software I used/developed here, although that is a big part of the project. I will compare two different magnetic measurement methods to the oversampling technique, and then try to see how different measurement parameters affect the outcome.

1.3 Goals and framework

1.3.1 Goals

The goal of the project is to verify that the method of combining rotating coil measurement works, by using it to measure a large-aperture and low-field magnet. Then I will look into how the different controllable parameters affect the outcome to establish some guidelines for good combinations of measurement parameters.

1.3.2 Framework

The time limit of the project is from my starting date at CERN, 1 February 2022, until the date set by NTNU as the deadline, which is 1 March 2023 at 12:00. The Rotating-Coil Mapper were finished around December 2022, meaning that I couldn't start to do measurements before then.

1.4 Thesis structure

The thesis is meant for reading sequentially from chapter to chapter. To make the page layout more concise, most tables with results are given in the Appendix, together with a Python script used for simulations and some matrix calculations also used in the post-processing of the actual data, showing the code behind the mathematical method. Here is a short description of each chapter;

Theory

A summary of the used theory for the thesis, from principles of magnetic measurement to a review of mathematical concepts such as matrix properties.

First, the basis for the thesis is laid out: the concept of a multipolar expansion of a magnetic field, and how to combine these using matrices. Then the chapter moves into measuring magnetic fields using induction, and some concepts used in the measurement.

Method and setup

The method and setup chapter first establishes good values for some parameters and explain known systematic errors and how they were treated.

Next, the chapter moves on to the actual measurement setup, a description of how the system works, together with the challenge of obtaining a reference measurement to compare the proposed method to, together with the reference measurement itself.

Analysis

This chapter starts with validating the proposed method, where a comparison between the reference measurements and the results from the proposed method is laid out. Then it moves into an analysis of the results and a look into how the different parameters used influence the results. Lastly, a short measurement done in a non-valid domain is carried out, with a look at the uncertainty.

Conclusion

A small summary of the results, what their impact will be in the future, and some suggestions for improving the method further.

Chapter 2

Theory

2.1 Circular accelerators and particle beam optics

Circular particle accelerators' (synchrotrons) working principle is by boosting a particle's energy by each turn, and by keep making turns as long as necessary until the required energy is reached. In a circular accelerator, there is a designed orbit on which ideally all particles should travel. To achieve this, bending forces are required to steer the beam in the wanted direction.

The Lorentz-force equation gives the definition of the force a charged particle **q** experiences when traveling with a speed **v** in an electric field **E** and a magnetic field **B**;

$$F = q\vec{E} + q(\vec{v} \times \vec{B}) \tag{2.1}$$

From the equation, the magnetic field only can act perpendicular to the direction the particle travels due to the cross product in the formula, as illustrated by figure 2.1. Thus, the motivation for magnetic measurements in particle accelerators is to precisely control the beam. The magnetic field is used to either bend the beam or to focus it.
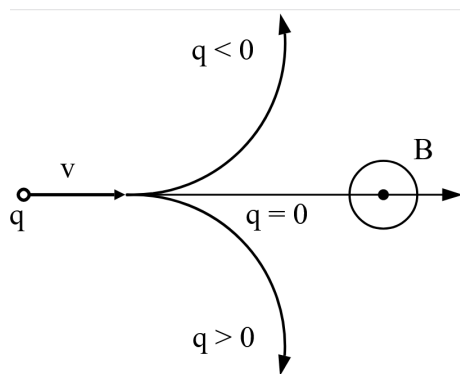
Figure 2.1: Illustration of the trajectory a particle q with a speed v under the influence of a magnetic field B. Illustrated for positive, negative, and neutral q. Taken from [7]

The bending of the beam is achieved by the use of a dipole magnet. The particle enters the magnetic field and then is bent inward towards the circular particle-accelerators center. The strength of the magnetic field dictates how much bending is achieved. Its curious to note that even though the magnetic field does not increase the particle energy, the maximum particle energy is nevertheless fixed by the maximum magnetic field (and the synchrotrons radius), since if there is too little bending, the particle will crash into the magnet-aperture.

The E-field could in theory be used to steer the particles, but considering that for speed $v \approx c$, and for a relatively small field of 1 T, an equivalent electric field would have a value of $3 \cdot 10^8 V m^{-1}$. Therefore it is not feasible in practice, and transverse magnetic fields are used instead.

However, E-fields are used to accelerate the particles, by injecting the particles into radiofrequency cavities where they receive an electrical impulse. Inside these cavities, the field is oscillating at a given frequency, so timing the impulse on the particles is important. In the LHC, the field is tuned to 400MHz [8], so when the beam has reached the required energy, a particle with the right energy will not be accelerated. However, a particle with slightly different energies arriving earlier or later will then be accelerated/decelerated so they stay close to the desired energy. The effect is that the particles get sorted into packs of particles called "bunches", with a spacing between them dependent on the radiofrequency-cavities frequency.

An estimation of the equation relating the magnetic field **B**, the curvature radius ρ and the particle momentum **p** is given by

$$\mathbf{p} = e\mathbf{B}\rho \tag{2.2}$$

During the acceleration of particles, the increase of particle momentum and the magnetic field is synchronized so the radius ρ stays the same.

2.1.1   Particle beam optics

Consider a particle moving along a circular orbit given by equation 2.2. Defining the coordinate system where s is along the circular orbit, and the xy-plane is the transverse plane to the circular orbit. The concept of a quadrupole magnet (a magnet with four poles) is also introduced here. A quadrupole magnet gives the following forces, proportional to the distance of the center of the orbit

$$B_y(s) = G_x \tag{2.3}$$
$$B_x(s) = G_y$$
$$B_s(s) = 0$$

with $0 < s < l_{magnet}$. Inserting this into the Lorentz-force equation, the following two equations show the force on a particle in both planes

$$F_x = e[\vec{v} \times \vec{B}]_x = -e\frac{ds}{dt}G_x \tag{2.4}$$

$$F_y = e[\vec{v} \times \vec{B}]_y = e\frac{ds}{dt}G_y \tag{2.5}$$
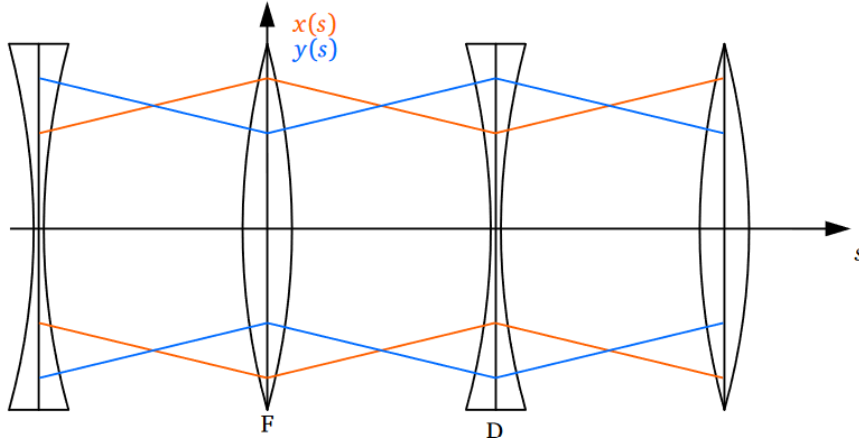
Figure 2.2: Illustration of a FODO-cell, with the transverse oscillations of the particles shown in blue and orange curves. Illustration taken from [9]

The equations is as expected similar, except for the sign. This means that one single quadrupole only can give linear stability in one plane, and instability in the other plane. Here a transition from classical mechanics into relativistic mechanics is in place, and the term γ_r replaces the classical v

$$\gamma_r = \frac{1}{\sqrt{1 - \frac{v^2}{c^2}}} \tag{2.6}$$

thus changing the classical equation for momentum $\vec{p} = m\vec{v}$ into $\vec{p} = m\gamma_r\vec{v}$. Without going further into the derivation of the equations, as relativistic mechanics is outside the scope of this thesis, the equation(only for x is derived) now reads

$$F_x = m\gamma_r \frac{d^2 x}{ds^2}\left(\frac{ds}{dt}\right)^2 \tag{2.7}$$

Integrating the equation for radius, momentum, and magnetic field, it can be shown that the equations become

$$\frac{d^2 x}{ds^2} + \frac{G}{\mathbf{B}\rho}x = 0 \tag{2.8}$$

$$\frac{d^2 y}{ds^2} - \frac{G}{\mathbf{B}\rho}y = 0 \tag{2.9}$$

here the last term is the normalized magnetic gradient, governing the bending force on the particle depending on the position along the trajectory. It is now clear that by using a quadrupole magnet it is possible to focus the beam in one plane. Further, using a combination of quadrupole magnets where the configuration is focusing on one plane, then the next configuration focuses on the other plane, there are cases where linear stability is possible.
 In the particle-accelerator community, this is called a *FODO-cell* configuration(figure 2.2) and is the most used way to ensure that the particle beam follows the wanted trajectory in the xy-plane. A precise knowledge of the magnetic fields, both the dipole and quadrupole are needed

to ensure that the beam moves along on a wanted trajectory. Higher-order magnets also have used in particle accelerators, but their use and explanation are beyond the scope of the thesis, nevertheless, the argument for tight control on the influx of different poled magnets is clear.

As the next sections will explain, there is no such thing as a pure n-poled magnet since all magnetic fields have some distortions representing forces found in different polar magnets. Combining both facts; that no magnet is ideal, and that in particle accelerators absolute control on the different poled magnets is needed, the need for an exact way to quantify magnetic multipoles emerges.

2.2 Multipolar expansion of magnetic field

This section is based on the method explained in CERNs "*Masterclass: Design of superconducting magnets for particle-accelerators*" [10] and Stephan Russenschucks book "*Field Computation for Accelerator Magnets*" [9]

The aim of the section is to show how one can decompose the measured voltage signal generated from a magnetic field into a set of Fourier harmonics.

Inside the bore of a magnet, assuming it is free of charge, the two following Maxwell equations hold true;

$$\nabla \cdot B = 0 \qquad\qquad \nabla \times B = 0 \tag{2.10}$$

Assuming that the length of the magnet is much larger than the diameter, the following statement is true inside the aperture $\frac{\partial B_z}{\partial z} = 0$ thus allowing to only consider the xy-plane. Developing the equations into Cartesian coordinates they become;

$$\frac{\partial B_x}{\partial B} - \frac{\partial B_y}{\partial y} = 0 \qquad\qquad \frac{\partial B_x}{\partial y} - \frac{\partial B_y}{\partial x} = 0 \tag{2.11}$$

Recognising that these two equations are the Cauchy-Riemann[1] conditions, the field can be defined as

$$B = B_y(x, y) + iB_x(x, y) \tag{2.12}$$

The Cauchy-Riemann theorem states that if the conditions are met, a function of a complex variable is holomorphic, which implies that it can be written as a complex power series (note that here $C(z)$ is the absolute value of the multipoles, and $z = x + iy$).

$$C(z) = B_y(x, y) + iB_x(x, y) = \sum_{n=0}^{\infty} C_n z^n \tag{2.13}$$

The coefficient C_n are the field harmonics, where the real and imaginary part represents the normal and skew components(vertical and horizontal).

$$C_n = B_n + iA_n \tag{2.14}$$

---

[1]https://en.wikipedia.org/wiki/Cauchy-Riemann_equations, visited March 2022

It is standard practice to introduce a reference radius R_{ref} which is usually set equal to 2/3 of the magnet aperture radius. The equation is now complete in the Cartesian coordinate system;

$$C(z) = B_y(x,y) + iB_x(x,y) = \sum_{n=0}^{\infty}(B_n + iA_n)(\frac{x+iy}{R_{ref}})^{n-1} \tag{2.15}$$

By changing $x+iy$ with $e = r_0 e^{i\theta}$ and applying some trigonometric substitution [6, p. 38], one can end up with an equivalent equation, where one clearly sees that the formula is another way of expressing the Fourier-components of the magnetic field.

$$B_r(r,\theta) = \sum_{n=0}^{\infty}(B_n \sin\theta n + A_n \cos\theta n) \tag{2.16}$$

The order n of the component corresponds to a magnetic field with $2n$ poles. A C_1 component corresponds to a magnet with order n, or $2 \cdot 1$ poles, namely a dipole, $n = 2$ corresponds to a magnet with $2 \cdot 2$ poles, namely a quadrupole and so forth. Further in the thesis the numerical order and the corresponding magnetic component will be used interchangeably.

Instead of representing the magnetic field on the domain as a continuous $\mathbb{R}^2 \mapsto \mathbb{R}^2$ function, it is possible to instead use an infinite complex Fourier-series and greatly reduce the information needed to describe the field, and later in the thesis, it will be clear that only the first 15-20 components of the infinite Fourier-series is needed for a sufficient description of the field. The Fourier coefficients are given by:

$$A_n = \frac{1}{\pi}\int_0^{2\pi} B_r(r_0,\phi)\cos(n\phi)\partial\phi$$
$$B_n = \frac{1}{\pi}\int_0^{2\pi} B_r(r_0,\phi)\sin(n\phi)\partial\phi$$

Normalization

In practice, the field harmonics are normalized to the main field component and multiplied by 10^4. The resulting values are dimensionless and called *units*. When normalized the term C_n are written in lowercase such that

$$C(z) = B_y(x,y) + iB_x(x,y) = 10^{-4}B_M \sum_{n=0}^{\infty}(b_n + ia_n)(\frac{x+iy}{R_{ref}})^{n-1} \tag{2.17}$$

The normalization by a main field component is given by

$$c_n := \frac{10^4}{B_M}C_n \tag{2.18}$$

where the number M is the order of a main field component, so that in the case for a dipole $M = 1$ and for a quadrupole $M = 2$, etc.

Allowed multipoles

A consequence of Gauss's law for magnetism which states that the magnetic field has divergence equal to zero, or that the magnetic flux through a field always must be zero, is that magnetic monopoles do not exist.

$$\nabla \cdot B = 0 \tag{2.19}$$

This means that all magnets will have some multipoles, no matter how good the design is. Due to symmetries in magnetic design, each type of magnet will have some multipoles that occur naturally, and these are called *allowed multipoles*. The general formula for allowed multipoles for a magnet with order M is $m = M(2n + 1)$. For a dipole magnet ($M = 1$), the first allowed harmonic is then the C_3 component, which corresponds to a sextupole field.

Motivation for multipolar expansion

The normalized multipoles can be viewed as an error in terms of the main field component. Doing a measurement of a magnet in this way gives some information on how *good* the magnet is. The non-allowed multipoles are coming from errors in magnet design or mechanical defects, and should ideally be zero.

Consider the case for the LHCs dipole magnets. In an ideal case, the magnets should have one multipole component, namely the C_1, and all others set to zero. This is as explained not possible, and therefore a precise measurement of each magnet is needed to know if the field harmonics are tolerable or need to be corrected. If a dipole magnet has too large a C_2 component, which can be viewed as a quadrupole magnet, the trajectory of the particle can be altered and the beam stray out of the given orbit and thus be lost.

2.2.1   Feed-down correction

A source of error in measurement is a misalignment of the coil rotational axis and the magnetic-field center, which can happen either due to insufficient precision, not knowing where the center is, or simply wanting to measure outside of the center. By doing several measurements and linking them, one can either find the magnetic center or link the measurements in a common reference frame.

$$\sum_{n=1}^{\infty} C_n(z_0) \left(\frac{z}{R_{ref}} \right)^{n-1} = \sum_{n=1}^{\infty} C_n'(z_i) \left(\frac{z'}{R_{ref}} \right)^{n-1} \tag{2.20}$$

Here z is the position in the normal reference frame, and z_i is the position with a non-normal reference frame. From figure 2.3 it is clear that $z = z' + z_i$, using this together with a binomial-series expansion, the equations can be further developed. $C_n\prime$ is for the following calculations the multipoles measured at a displaced position.
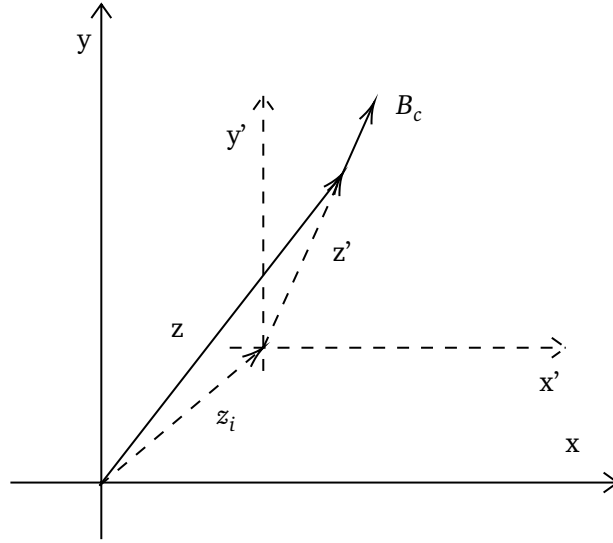
Figure 2.3: The complex magnetic field B_c in the original and displaced reference frame.

$$\sum_{n=1}^{\infty} C_n(z_0) \left(\frac{z}{R_{ref}} \right)^{n-1} = \sum_{n=1}^{\infty} C_n(z_0) \left(\frac{z' + z_i}{R_{ref}} \right)^{n-1}$$

$$= \sum_{n=1}^{\infty} \sum_{k=1}^{n} C_n(z_0) \binom{n-1}{k-1} \left(\frac{z'}{R_{ref}} \right)^{k-1} \left(\frac{z_i}{R_{ref}} \right)^{n-k} \tag{2.21}$$

Knowing the identity (taken from [11])

$$\sum_{k=0}^{\infty} \sum_{n=0}^{k} t_{kn} = \sum_{n=0}^{\infty} \sum_{k=n}^{\infty} t_{kn} \tag{2.22}$$

and that $\binom{a}{b} = \binom{a}{a-b}$, equation 2.21 can be rearranged into

$$C'_n(z_i) = \sum_{k=n}^{\infty} C_k(z_0) \binom{k-1}{k-n} \left(\frac{z_i}{R_{ref}} \right)^{k-n} \tag{2.23}$$

giving an equation for multipoles in a displaced reference frame, in terms of the multipoles at the magnetic center which is represented by $C_k(z_0)$.

For low order multipoles, or if $|z_i| \ll R_{ref}$ the series converge fast. Considering that the multipoles generally are three or four orders of magnitude lower than the main component, it is clear that the effect is most significant on the harmonic below the main component. This is called the feed-down effect since the higher-order harmonics affect the lower ones.

2.2.2 Combining rotating coil measurements

The field harmonics are given for a reference radius, and changing the radius will directly change the field harmonics. To compare multipoles with different reference radii, they need to be scaled accordingly. This is done by using equation 2.15

$$\sum_{n=1}^{\infty} C_n(r_1)\left(\frac{z}{r_1}\right)^{n-1} = \sum_{n=1}^{\infty} C_n(r_2)\left(\frac{z}{r_2}\right)^{n-1} \tag{2.24}$$

Comparing the coefficient C_n of the series expansion

$$\frac{C_n(r_1)}{r_1^{n-1}} = \frac{C_n(r_2)}{r_2^{n-1}} \rightarrow C_n(r_2) = \frac{r_2}{r_1} \cdot C_n(r_1) \tag{2.25}$$

By using equation 2.23 and 2.25 together one can then get a general formula allowing to measure several places inside the field, and then combine them in a common reference frame.

The left side of both equations is the same, and one can compare

$$C_n'(r_0, z_i)\left(\frac{r_0}{r_c}^{n-1}\right) = \sum_{k=n}^{K} C_k(z_0)\binom{k-1}{k-n}\left(\frac{z_i}{R_{ref}}\right)^{k-n} \tag{2.26}$$

$$\Rightarrow C_n'(r_0, z_i) = \sum_{k=n}^{K} C_k(z_0)\binom{k-1}{k-n}\left(\frac{z_i}{R_{ref}}\right)^{k-n}\left(\frac{r_c}{r_0}\right)^{n-1}$$

note that here the variable $C_n'(r_c, z_i)$ is the multipoles measured at the position z_i with the coil radius r_c.

Equation 2.26 give a way to convert a measured multipole $C_n'(r_c, z_i)$ into multipole $C_k(r_0, z_0)$ at the center with a reference radius r_0 and position z_0. To find the unknown multipoles C_k at least $K-1$ equations is needed to determine them. One can therefore do enough measurements at different positions to find a solution, and thus the endpoint will be a matrix formalism of the equation system. An overview of the different variables used for the combination of multipoles onto a common reference radius is given in table 2.1.

For better readability one can apply

$$w_{n,k}^{(i)} = \binom{k-1}{k-n}\left(\frac{z_i}{R_{ref}}\right)^{k-n}\left(\frac{r_c}{r_0}\right)^{n-1}$$

thus ending up with

$$C_n'(r_c, z_i) = \sum_{k=n}^{K} w_{n,k}^{(i)} C_k(r_0, z_0) \tag{2.27}$$

N	Highest order multipole acquired by the small coil
K	Number of reconstructed multipoles on the reference radius
I	Number of measured positions
n	Multipole order of measurement with small coil, $n \in [2, N]$
k	Multipole order of field reconstruction on the reference radius, $k \in [2, K]$
i	Enumerator for the measured position, $i \in [1, I]$
C'_n	Measured multipoles on small shaft
C_k	Reconstructed multipoles on the reference radius
z_i	Position of the measurement in the complex plane

Table 2.1: Overview of the variables

Now the sum can be written for different measurement positions z_i and different multipole orders n;

$$C'_2(r_c, z_1) = w^{(1)}_{2,2} C_2(r_0, z_0) + w^{(1)}_{2,3} C_3(r_0, z_0) + \cdots + w^{(1)}_{2,K} C_K(r_0, z_0)$$

$$C'_3(r_c, z_1) = w^{(1)}_{2,2} C_2(r_0, z_0) + w^{(1)}_{3,3} C_3(r_0, z_0) + \cdots + w^{(1)}_{3,K} C_K(r_0, z_0)$$

$$\vdots$$

$$C'_2(r_c, z_2) = w^{(2)}_{2,2} C_2(r_0, z_0) + w^{(2)}_{2,3} C_3(r_0, z_0) + \cdots + w^{(2)}_{2,K} C_K(r_0, z_0)$$

$$C'_3(r_c, z_2) = w^{(2)}_{2,2} C_2(r_0, z_0) + w^{(2)}_{3,3} C_3(r_0, z_0) + \cdots + w^{(2)}_{3,K} C_K(r_0, z_0)$$

$$\vdots$$

$$C'_N(r_c, z_I) = w^{(I)}_{N,K} C_2(r_0, z_I) + w^{(I)}_{N,K} C_3(r_0, z_I) + \cdots + w^{(I)}_{N,K} C_K(r_0, z_I)$$

The system of equations can now be written as a matrix

$$\{C'\} = [M]\{C\} \tag{2.28}$$

where the matrix $[M] \in \mathbb{C}^{(N-1)I \times (K-1)}$ are the radii, measurement position and the binomial coefficients of the series representation. $\{C'\} \in \mathbb{C}^{(N-1)I}$ is the complex valued measured field harmonics, and $\{C\} \in \mathbb{C}^{K-1}$ contains the multipoles in the reference frame. Expanding $\{C'\}$ and $\{C\}$ the following emerges

$$\{C'\} = (C'_2(z_1), C'_3(z_1), \cdots, C'_N(z_1), C_1(z_2), \cdots)^T$$

$$\{C\} = (C_2, C_3, \cdots C_K)^T$$

The matrix $[M]$ is composed of I inner matrices, each corresponding to a measurement position

$$[M] = \begin{pmatrix} [W_1] \\ \vdots \\ [W_i] \\ \vdots \\ [W_I] \end{pmatrix} \tag{2.29}$$

and where the inner matrices holds the information from equation 2.27

$$[W_i] = \begin{pmatrix} w_{2,2}^{(i)} & \cdot & \cdot & \cdot & \cdot & \cdots & w_{2,K}^{(i)} \\ 0 & \cdot & \cdot & \cdot & \cdot & \cdots & \cdots \\ 0 & 0 & \cdot & \cdot & w_{n,k}^{(i)} & \cdots & \cdots \\ \vdots & \vdots & \ddots & w_{n,k}^{(i)} & \cdot & \cdots & \cdots \\ 0 & 0 & 0 & 0 & \cdots & w_{N,K-1}^{(i)} & w_{N,K}^{(i)} \end{pmatrix} \tag{2.30}$$

The matrix M is over-determined, and an over-determined system has an infinite number of solutions. To solve this system for $\{C\}$, the method of Least-Squares is applied.

Condition number

The condition number κ of a matrix **M** measures how much a small change in the input value affects the output. It is also a measurement of how close the matrix is to being *singular*, which then again implies that one or several rows or columns are close to being a linear combination of other rows or columns.

Given an equation system $Ax = B$, the condition number is the maximum ratio of the relative error in x to the relative error in b. For a normal matrix A, then the condition number is given as

$$\kappa(A) = \frac{|\sigma_{max}(A)|}{|\sigma_{min}(A)|} \tag{2.31}$$

where $|\sigma_{max/min}(A)|$ is the max/min of the eigenvalues of the matrix.

As a general rule, if the condition number $\kappa(\mathbf{M}) = 10^n$, then one may lose up to n digits of accuracy. Therefore, it follows one wants to keep the condition number low.

2.2.3 Decay and sampling rate

Multipole decay

Using Biot-Savarts law, and applying it to the field of an infinite current line, one end up with the following identity [10]

$$B(r) = \frac{u_0 I}{4\pi} \int_{\infty}^{\infty} \frac{ds}{s^2 + r^2} = \frac{u_0 I}{2\pi r} \tag{2.32}$$
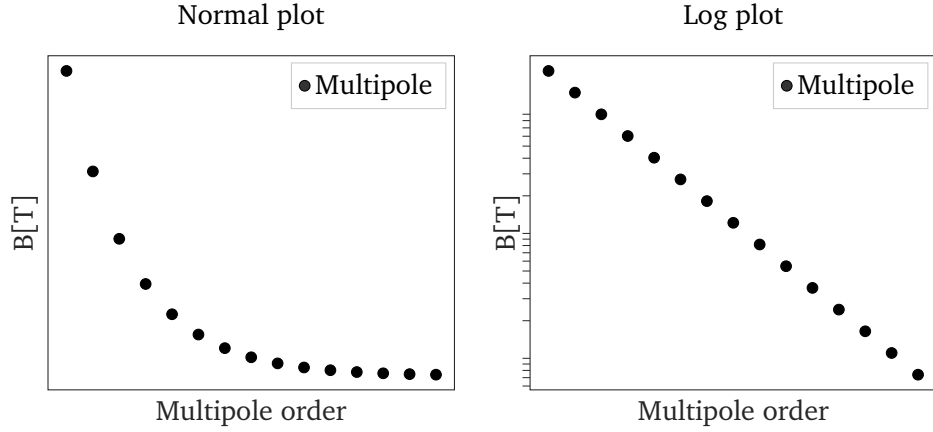
Figure 2.4: Multipole decay seen from a plot of the first 15 multipoles

which it can be shown is equal to the following equation in Cartesian coordinates[10]

$$B_y + iB_x = -\frac{u_0 I}{2\pi z_0} \sum_{n=1}^{\infty} \left(\frac{z}{z_0}\right)^{n-1} \tag{2.33}$$

From here equation 2.15 can be used to deduce the decay (or *scaling-law*) of the multipoles. Note that the factor $10^{-4}B_1$ is introduced, which is to normalize the units of the multipoles. Combining equation 2.15 and equation 2.33 gives

$$B_y(x,y) + iB_x(x,y) = 10^{-4} B_1 \sum_{n=0}^{\infty} (b_n + ia_n) \left(\frac{z}{R_{ref}}\right)^{n-1} \tag{2.34}$$

$$-\frac{u_0 I}{2\pi z_0} \sum_{n=1}^{\infty} \left(\frac{z}{z_0}\right)^{n-1} = 10^{-4} B_1 \sum_{n=0}^{\infty} (b_n + ia_n) \left(\frac{z}{R_{ref}}\right)^{n-1}$$

Rearranging and taking the logarithm on both sides yields

$$(b_n + ia_n) = -\frac{10^4}{B_1} \frac{u_0 I}{2\pi z_0} \left(\frac{z}{R_{ref}}\right)^{n-1}$$

$$(b_n + ia_n) = -\frac{10^4}{B_1} \frac{u_0 I}{2\pi R_{ref}} \left(\frac{R_{ref}}{z_0}\right)^{n}$$

$$\ln|b_n + ia_n| = \ln\left(\frac{10^4}{B_1} \frac{u_0 I}{2\pi R_{ref}}\right) + n \ln\left(\frac{R_{ref}}{z_0}\right) \tag{2.35}$$

It is clear to see from the equation that the multipoles must decay as a power law, or if plotted semi-logarithmic, as the ratio between the reference radius and position z as shown in figure 2.4.

These results can be used to verify the consistency of the measurements. In practice, the multipoles do not form a perfect line when plotted semi-logarithmic. From the plot, one can see if the slope is consistent with the ratio $\frac{R_{ref}}{z_0}$, and one can also estimate the precision of the system by looking at the spread of values. An illustration of this decay is given in figure 2.4.

From equation 2.16 it is clear to see that the multipoles grow exponentially if one is outside the reference radius $z > R_{ref}$, or as shown from Biot-Savart's law (eq 2.33) that they decay exponentially the farther they are from their source, in this case, the magnet aperture.

Sampling rate

One should note that equation 2.16 is only valid for a continuous B_r, which doesn't exist in practice since the equipment is sampling in discrete time. Therefore the Discrete Fourier-Transform is needed, and the coefficients then become;

$$A_n(r_0) \approx \frac{2}{N} \sum_{k=0}^{N-1} B_r\left(r_0, \frac{2\pi k}{N}\right) \cos n\frac{2\pi k}{N} \tag{2.36}$$

$$B_n(r_0) \approx \frac{2}{N} \sum_{k=0}^{N-1} B_r\left(r_0, \frac{2\pi k}{N}\right) \sin n\frac{2\pi k}{N} \tag{2.37}$$

Where k is the number of sinusoidal cycles per N samples. One has to decide how many samples N is needed for the measurements to give a satisfactory precision.

Since the aim is to measure only the first 15-20 multipoles, the *Nyquist-Shannon*[12] theorem can be applied, which tells how many samples is needed to bridge the gap between continuous-time signals and discrete-time signals.

$$x(t) = \sum_{n=-\infty}^{\infty} x_n \frac{\sin(\pi(2Bt - n)}{\pi(2Bt - n)} \tag{2.38}$$

This states that to get a perfect reconstruction of a function x(t) a sampling rate above 2 times the function's highest frequency is sufficient. Since one already know that the aim is to measure the first 15-20 multipoles, and it rapidly converges after that, the sampling rate can be deduced.

Here is a reminder that a Fourier analysis can be viewed as decomposing a time-domain signal into a frequency-domain is in place, and that multipoles essentially are frequencies. Coupling that with the Nyquist-Shannon theorem, one, therefore, want a sampling rate greater than 2B, where B is the highest-order multipole one wants to measure, thus giving a rate greater than $20 \cdot 2 = 40$ samples.
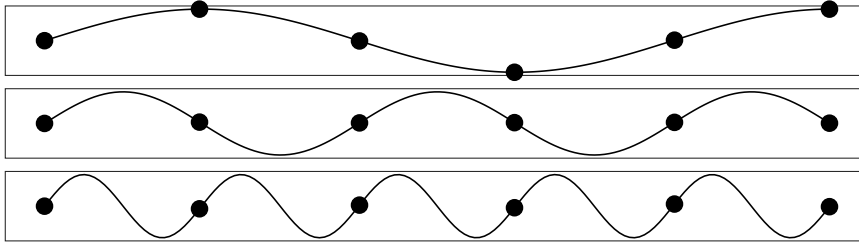
Figure 2.5: Illustration showing how the sampling size needs to be greater than 2B the frequency to recreate a signal, sampling rate of 2Hz, first wave 1Hz, second wave 2Hz, third wave 3Hz. Notice how only the first graph has enough samples to reconstruct the given curve

2.3 Measuring magnetic fields with induction

A commonly used technique for measuring magnetic fields and their properties is by using a conductive material inside a magnetic field. Thus, one can move the material around inside the field, or change the magnetic field with respect to time, to induce a voltage proportional to the change in flux, as described by Faraday's law of induction. This is the most common method of measuring the magnetic field of magnets at CERN. For the next sections, a rotating coil is used as an example of the material in the voltage is induced in.

$$\varepsilon = -\frac{\partial \Phi}{\partial t} \tag{2.39}$$

Solving Faraday's law for ϕ gives the following integral, which describes the magnetic flux through a surface.

$$\Phi = -\int_{t_1}^{t_2} \varepsilon \, dt \tag{2.40}$$

FDI: Fast Digital Integrator

To get the magnetic flux from equation 2.40 a time-dependent integral must be solved. To do this, a Fast Digital Integrator was developed at CERN. The working principle is an integration of the analog voltage signal in the digital domain, to minimize the noise from analog uncertainty sources. This work together by a trigger source such as pulses coming from an angular encoder, which tells the FDI when to integrate. In the case of a coil as the conductive material, the signal is sampled in a discrete series of $\mathcal{N}$ points, meaning all of the points $\mathbf{p} \in [1 \dots \mathcal{N}]$.

$$\Delta \Phi = \Phi(t_2) - \Phi(t_1) = -\int_{t_2}^{t_2} V \, dt \tag{2.41}$$

By changing t_1 and t_2 with θ_1 and θ_2, which is the flux when the integration starts and the flux when the integrator receives another trigger, the equation is parameterized away from being dependent on time to being dependent on angular position instead.

$$\Delta \Phi = \Phi(\theta_2) - \Phi(\theta_1) \tag{2.42}$$

By doing this, one can reduce the uncertainty arising from time-dependent variables, such as not having perfectly uniform coil rotational speed when using the rotating coil method[13].

2.3.1 Flux linkage

Here the derivation of the flux linkage is laid out, which is the link between the flux and the complex field. The flux linkage also gives a seamless transition into the coil's sensitivity factors, which will be explained in the next section.

Given an induction coil with N turns, area A, and length L, the linked magnetic flux can be calculated as the integral of the magnetic field over the area spanned by the wire loop

$$\phi = \int_A \vec{B} \cdot d\vec{A} = \int_0^L \int_{P1}^{P2} \vec{B} \cdot d\vec{n} \, dl \tag{2.43}$$

The vector $\vec{n}$ points normally to the direction out of the spanned area. The vector $d\vec{s}$ is defined as the vector that points from P1 to P2. It is orthogonal to $\vec{n}$ and rotated by $\frac{\pi}{2}$.

$$d\vec{s} = \begin{pmatrix} dx \\ dy \end{pmatrix} = \begin{pmatrix} -dn_y \\ dn_x \end{pmatrix} \tag{2.44}$$

Thus one can write $B \cdot d\vec{n} = B_x dy - B_y dx$, which also equals the real part of the product $-(B_y + B_x i)(dx + idy)$. Writing out the full product gives

$$-(B_y + B_x i)(dx + idy) = B_x dy - B_y dx - i(B_y dy + B_x dx) \tag{2.45}$$

This allows transforming the vectorial 2.43 into the complex domain. Substituting dz for the complex equivalent $d\vec{z}$, and noting that the real part of the product $-B(z)dz$ equals the scalar product $\vec{B} \cdot d\vec{n}$, gives the following equation

$$\phi = -\int_0^L Re \left\{ \int_{z_1}^{z_2} z(z)dz \right\} dl \tag{2.46}$$

z_1 and z_2 give the points P_1 and P_2 in the complex plane. It is common to change the order of the integrals and compute the real part afterward. Furthermore, since rotating coil measurements give a strictly two-dimensional representation of the magnetic field, there is no longitudinal resolution. In the final equation below a factor N_t for multiple turns of the coil is added

$$\phi = -N_t L Re \left\{ \int_{z_1}^{z_2} B(z)dz \right\} \tag{2.47}$$

Now, to be able to solve this integral analytically one can change the term $B(z)$ into the multipolar expansion from equation 2.16 to end up with

$$\phi = -N_t L Re \left\{ \sum_{n=1}^{\infty} \frac{C_n}{n r_0^{n-1}} (z_2^n - z_1^n) \right\} \tag{2.48}$$
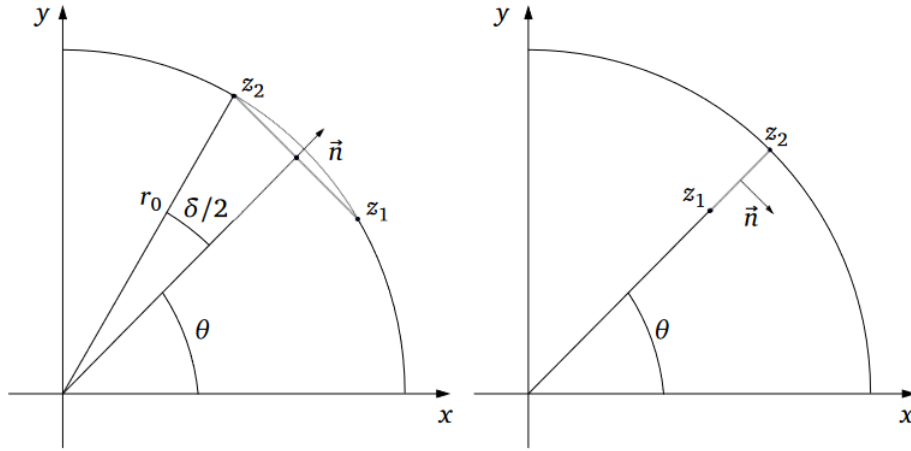
Figure 2.6: Illustration of the tangential(left) and radial(right) coil designs, note the different positions for the points z_1 and z_2. The figure is taken from [15]

It is now shown that the measured flux is linked to the multipole errors of the field and the coil design. Its straightforward to see that for different coil design each multipole will give different flux values. This is called coil sensitivity. Equation 2.48 is usually written in the following form, where K_n is the sensitivity factors

$$\phi = -Re\left\{\sum_{n=1}^{\infty} \frac{C_n}{nr_0^{n-1}}K_n\right\} \tag{2.49}$$

2.3.2 Sensitivity factors

The sensitivity factors K_n of a coil tell how capable it is to acquire a multipole of the n-th order [14], and is derived from the coil's geometric properties.

$$K_n := \frac{N_t L}{n}(z_2^n - z_1^n)e^{-in\theta} \tag{2.50}$$

where θ is the angle of the coil to the horizontal axis. Note that a rotation to the coil fixes both points Z_1 and z_2 to this angle, thus the sensitivity factors of the coil is independent of this value.

Several different coil designs exist, here a presentation of the two most common will follow, the radial and tangential coil designs.

Tangential coil design

A tangential coil has wound the wire on the outside of the shaft, as illustrated by the line spanning points z_1 and z_2 in the left drawing from figure 2.6 which is showing the cross-section of a tangential coil. Both points have the same radius r_c, and the angle δ is the angle between the two points. This angle δ is called the opening angle of the coils.
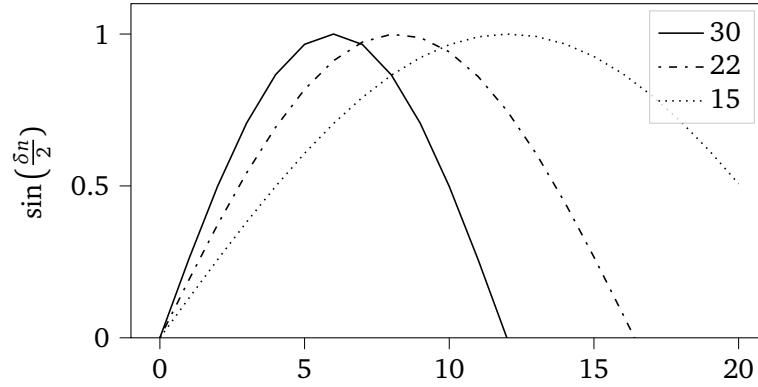
Figure 2.7: The term $sin(\frac{n\delta}{2})$ for the three angles 30°, 22°, 15°, showing which multipoles the opening are most (or least) sensitive to depending on how the sinusoidal period changes.

Developing equation 2.50 further for the tangential coil, one ends up with

$$
\begin{aligned}
K_n^{tan} &= \frac{N_t L}{n} r_c^n (e^{in\frac{\delta}{2}} - e^{-in\frac{\delta}{2}}) \\
&= 2\frac{N_t L}{n} r_c^n sinh(i\frac{n\delta}{2}) \\
&= \frac{2iN_t L}{n} r_c^n sin(\frac{n\delta}{2})
\end{aligned}
\tag{2.51}
$$

It is clear that a large coil radius r_c is needed for a high sensitivity factor. Further, the sensitivity factor is highly dependent on the opening angle δ. From figure 2.7 it is clear to see that changing the opening angle changes the sensitivity to certain multipoles drastically. For an opening angle $\delta = 30°$ the coil is most sensitive to the multipole order $n = 6$, but falls of fast, and at multipole $n = 12$, the sensitivity is zero.

When a coil has zero sensitivity to a multipole order it cannot measure the multipole, and opposite, when a coil has a high sensitivity to a multipole, the coil can measure it precisely. Making the opening angle smaller shifts the multipole order with zero sensitivity by the coil higher. The trade-off is lower sensitivity to all the lower-order multipoles in general.

Radial Coil

Shown to the right in figure 2.6 is the layout of a radial coil cross-section. In a radial coil the coil wires are mounted at different radii, but at the same angle as illustrated by the points z_1 and z_2 in the figure. The position of both coils is given by
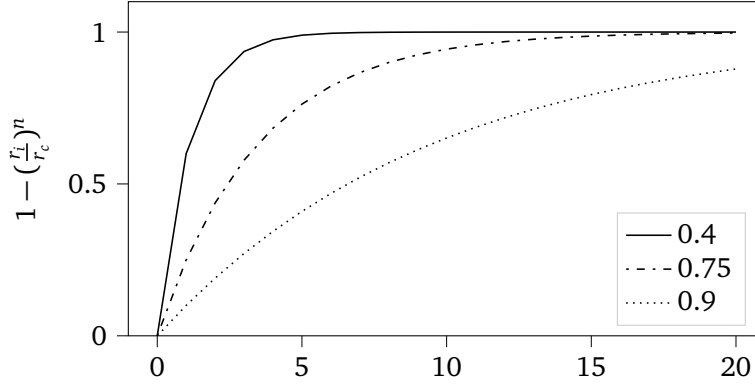
Figure 2.8: Sensitivity factor of different $\frac{r_i}{r_c}$ in a radial coil

$$z_1 = r_{z_1} e^{i\theta}$$
$$z_1 = r_{z_2} e^{i\theta} \tag{2.52}$$

Developing the sensitivity factors for the radial coil by inserting the positions

$$K_n^{rad} = \frac{N_t L}{n}(r_{z_2}^n - r_{z_1}^n) \tag{2.53}$$

using this result, the flux from equation 2.49 becomes

$$\phi = -Re\left\{ N_t L \sum_{n=1}^{\infty} \frac{C_n}{nr_0^{n-1}}(r_{z_2}^n - r_{z_1}^n)e^{in\theta} \right\} \tag{2.54}$$

It is common practice to express the multipoles at the outermost radii, therefore the reference radius r_0 is set to r_c, which yields the following equation

$$\phi = -Re\left\{ N_t L \sum_{n=1}^{\infty} \frac{r_c C_n}{n}\left[1 - \left(\frac{r_i}{r_c}\right)^n \right]e^{in\theta} \right\} \tag{2.55}$$

Now it is trivial to see that the term

$$\left[1 - \left(\frac{r_i}{r_c}\right)^n \right] \tag{2.56}$$

governs the sensitivity to a multipole of order n. This value always falls between 0-1. From figure 2.8 this configuration looks optimal as it has no trade-offs in the analytic sense, and the sensitivity increases monotonically with multipole-order. However the manufacturing process is difficult[16], but recent advances in PCB technology have made this approach feasible for the CERN laboratories.

2.3.3 Bucking

The rotating coil system is prone to uncertainty, such as acquisition noise, and vibrations, or mechanical uncertainty such as sag in the materials used for the coil. However, the benefit of using a rotating coil system is the possibility to reduce some of these uncertainties. CERN uses PCB probes for coils, to reduce uncertainty in geometries of regular coils, and with the PCB technique one can reproduce effective coil area with a relative error on the order of 10^{-4} [17]. Usually, several PCB coils together inside a non-magnetic material make up a complete coil shaft. Since several coils make up the shaft mechanical errors such as vibrations affect them in the same way.

A common technique to achieve finer accuracy when measuring magnetic multipoles is called *bucking*. The main idea is to use sets of coils with contrasting geometries or varying properties to cancel out some harmonics, thus achieving greater sensitivity to other multipoles. This is done by taking the differential signal of two or more coils in different configurations.

To illustrate the concept more clearly, the center of a dipole-magnet is used as an example and the process is illustrated in figure 2.9. Using equation 2.15 the terms are given by

$$B_y + iB_x = \sum_{n=1}^{\infty} C_n(r_0)\left(\frac{z}{r_0}\right)^{n-1} \tag{2.57}$$

Here $z = x + iy$ and $C_n = B_n + iA_n$. The first harmonic, representing the dipole component will be $C_1(r_0)$, due to raising the parenthesis to the power $n-1 = 0$, which makes it one. The other harmonics will be zero in the center, due to $z = 0$.

$$B_1 = \sum_{n=1}^{\infty} C_n(r_0) \tag{2.58}$$

$$B_2 = \sum_{n=1}^{\infty} C_n(r_0)\left(\frac{0}{r_0}\right)^{2-1} = 0 \tag{2.59}$$

Following the equation, all the multipoles decrease fast from the magnetic poles, except for the dipole component which is nearly constant in the whole field. This fact can be exploited by having two identical radial coils, one coil **A** mounted in the middle, and one coil **B** mounted at the radii, having negative polarity from coil **A**. Coil **A** will only pick up the signal from the dipole component, while coil **B** picks up the signal from all field harmonics, including the second order. Since both coils are identical, the flux gained from the dipole component will be the same for both coils. If now signal **A** is analogy subtracted from signal **B** the second order is then in an ideal case removed from the signal, which means the sensitivity to higher order harmonics is increased, which is the same as increasing the signal-to-noise ratio. This can be extended to higher-order harmonics, but usually one aims to cancel the dipole and quadrupole-component.

Using bucking, the influence of mechanical errors such as sag and vibrations is reduced significantly. This is expected since the PCB probes all are affected in the same way by systematic
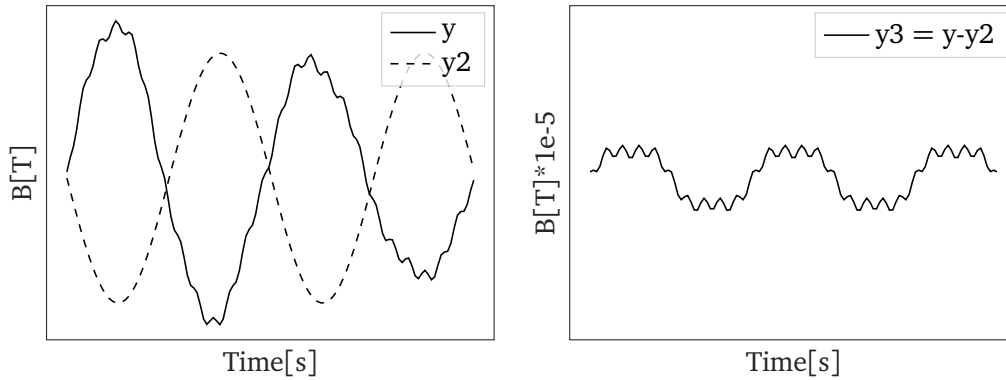
Figure 2.9: Visualization of bucking, **y** the signal from a coil sensitive to all harmonics, y_2 is the signal from a coil only sensitive to the dipole component, and then $y_3 = y + y_2$ which is the signal actually measured, are the higher order harmonics. In signal y_3 higher sensitivity to the harmonics is achieved

errors due to being on the same shaft. The PCB probes need to be geometrically identical for them to pick up the same flux, therefore this method is limited by the precision in replicating the PCB probes.

2.3.4 Single-Stretched Wire measurements

Wire measurements are done by having a tight wire mounted between two linear stages, where the wire goes through the magnet aperture, just as with the rotating coil method. The difference is that the wire also goes back either through the aperture, or outside, essentially forming a closed loop. Then, one can either move the wire through a static field or pulse the field while the wire is being kept constant.

The Single-Stretched Wire (SSW) measurement can be viewed as a rotating-coil measurement essentially doing one turn with the coil. The SSW measurement is flexible but can lack in signal-sensitivity. This means when there is a very low field, the signal acquired can be hard to distinguish from noise.

 Just as with the rotating coil method, the induced voltage is then digitally integrated with an FDI, and one can obtain multipoles from the field, or determine the magnetic center from the obtained field gradients. Unlike a rotating coil measurement, measuring with wires is not dependent on knowing the coil geometry to a fine level. Wire measurements will be introduced later in the thesis to calculate the coil geometry of the used coil, and to be used as a reference for the measurements.
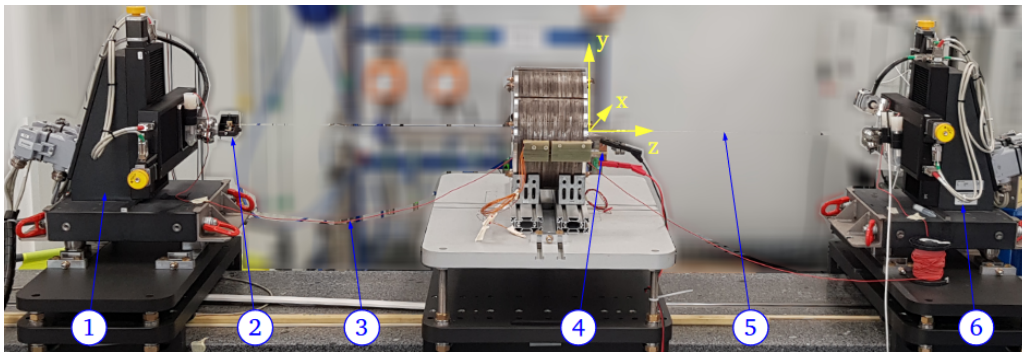
Figure 2.10: Single-Stretched Wire setup. A magnet is in the center, with the yellow coordinate system which is the same used for rotating coil measurements included. The picture shows 1,6) the linear stages moving the wire, 2) an optical sensor not used in the thesis 3) the return wire forming a closed loop, 4) power connectors and 5) the barely visible wire. Taken from [15].

Chapter 3

Proposed method and measurement setup

In this chapter, the proposed measurement challenges are laid out, along with the derivation and reasoning for the parameters used, together with ways to compensate for the known systematic errors. The first section looks into the number of measurement positions' effect on error propagation, and an argument for using lower-order multipoles to reconstruct the higher-order ones. This is done by several simulations written in Python and by experimental validation.

After an explanation of the measurement bench's setup is given, together with an overview of the post-processing of the raw signals. Then the chapter gives an overview of the chosen reference measurements and an explanation of why they were chosen.

3.1   Measurement parameters

The method of combining rotating coil measurements essentially lets the operator choose three parameters, namely the number of measurement positions I, the number of multipoles to use reconstructing the rest K, and the measurement radii. As explained in section 2.2.3 the multipoles decays fast from the magnet aperture, thus obviously implying one wants to measure as close to the aperture as possible. This leaves the effect of the two other parameters unknown and should be investigated to obtain the best possible results.

3.1.1   Number of measurement positions effect on error propagation

Since the method relies on doing several measurements and combining them, it is prone to measurement errors. For each measurement position introduced, there will most likely be an error, for instance, as the coil position is only known to a finite extent. Together with the positioning error, some noise will be captured in the measurements. Therefore it is important to see how the method responds to error propagation, and then try to minimize the effect it will have on the computed result.

For the following calculations, Python was used together with the Sci-Py kit [18], which has
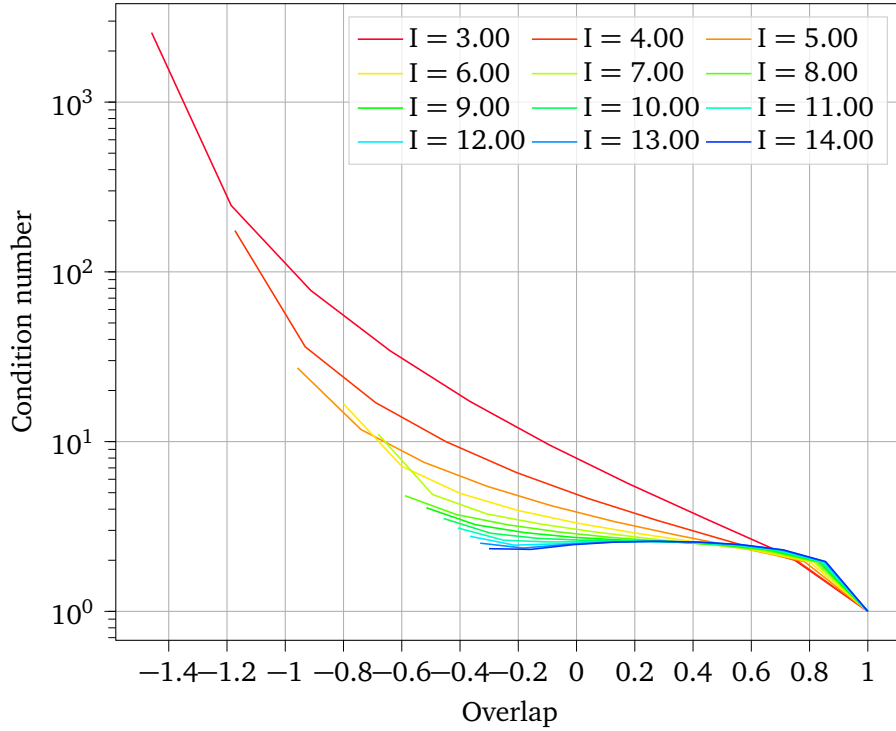
Figure 3.1: Condition number plotted against overlap between coil positions. Number of reconstructed multipoles on reference radius K = 15, and highest multipole acquired k = 15 for every simulation.

several algorithms in place for computing the following matrix properties. The script used is added in the Appendix (listing A.2).

Keeping the number of reconstructed multipoles constant at K=15 allows us to vary the number of measurements, and their relative position to each other. In figure 3.1 the condition number is plotted against the overlap for different numbers of measurements I.

The overlap is defined as the radius of the coils minus the distance between the center of two coils, divided by the coil radius. The negative overlap then coils far apart, and when the overlap is 1 they have the same center and radius. So for each measurement position I, the condition number is plotted for different overlaps. Since the overlap is defined to be distances divided by each other, the simulation is independent of the actual coil radius in physical units, and the number on the x-axis is then given as a ratio between the coil size and the overlap. Since each line is showing a constant number of measurement positions I, with different overlaps, going rightwards on each plot-line is essentially changing the given radii of the coils used.

In practice, since an infinite number of coils do not exist, it is not possible to vary the radii continuously, meaning some of the configurations will be unfeasible. Nonetheless, the simulation

gives a clear picture of how increasing the overlap between coils or increasing the number of measurement positions makes the condition number trend toward 1.

From figure 3.1 it is clear that the condition number shrinks by increasing the number of measurement positions, or by increasing the overlap between each measurement. This is expected if n measurements perfectly overlap each other, all capturing $K = k$ number of multipoles (which in this case is 15). The result is the identity matrix, whose condition number is 1.

It is clear that one generally wants to measure more than 8 positions ($I > 8$) and have less than -0.4 overlap to minimize the condition number (meaning keeping it under 10^1). Although the condition number is a good measurement for error amplification, too much importance should not be given to it. If the measurements don't introduce any noise, the condition number becomes irrelevant. Therefore, experimental validation of the method is needed in combination.

3.1.2   Number of multipoles acquired

The combination of the rotating coil measurements method allows for using the measured multipoles to reconstruct non-measured multipoles. The operator must then chose how many multipoles to reconstruct K, and how many multipoles the small coil acquires N.

Generally one want to use the lower-order multipoles to reconstruct the higher-order ones. The reason, as a byproduct of Cauchy's integral formula [9] [19], is that the field-harmonics decays logarithmically with the order. The value of the higher-order harmonics then becomes smaller than the equipment's noise floor, and the signal becomes indistinguishable from noise. As explained in section 2.2.3 this becomes visible if the multipoles are plotted semi-logarithmically, the noise floor is where the multipoles stop decaying linearly and flatten out. From figure 3.2 it is clear that the precision limits of the equipment are around multipole order $n \approx 6$. This varies for each configuration of magnet and coil used, and thus must be verified experimentally for every new configuration.

The method of combining rotating coil measurements has two benefits compared to using a single coil in the middle; the first is as discussed, the possibility of reconstructing the higher-order field harmonics using the lower ones, which is acquired with better precision. This is done by the Least-Squares fit in the combination algorithm.

The second benefit is that the method lends itself to measuring closer to the magnet aperture, and thus capturing the higher-order multipoles with higher precision due to being closer to their current source, as explained in section 2.2.3. Therefore, they might be measured with satisfactory precision directly.

Note that figure 3.1 is plotted for coils acquiring $N = 15$ multipoles, while this section argues that one should obtain $N = 5$ multipoles on each position instead. Since the number of multipoles obtained with satisfying precision depends on the coil used, the strength of the magnetic field, and random errors, using $N = 15$ multipoles for the plot gives a more generalized
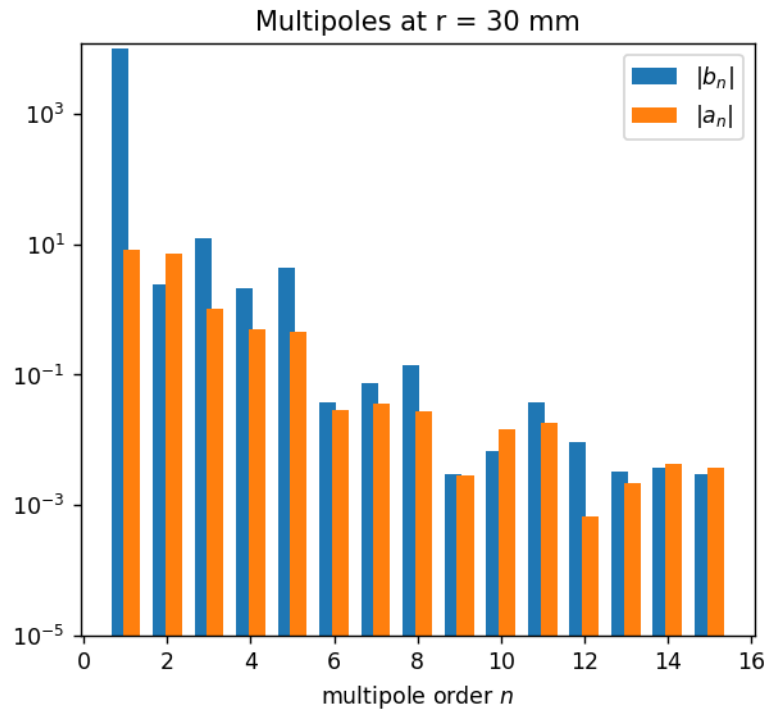
Figure 3.2: Multipoles measured with the coil in the center of the AirCoil-magnet in dipole mode and dipole bucking applied. The plot is the same as shown in section 3.4, and is the reference measurement obtained in a later section.

overview of the trend of the conditioning number, thus being applicable to more situations.

3.1.3   Number of coil turns impact on standard-deviation

For rotating coil measurements it is common to rotate the coil several times, and then take the average result. Therefore, the number of coil turns need to be decided to keep the standard deviation sufficiently low.

The calculated standard deviation here is only characterizing the rotation of the coil, for a single measurement. In section 4.1.4 the standard deviation is calculated for the whole method of oversampling measurements. From figure 3.3 one can see that the standard deviation rises with turns until it flattens out at 50 turns, where it is at 0.2 units. 20 turns of the coil at each position is chosen, given that increasing the turns to 50 means an increase in time of approximately 30 seconds, which an 0.1 decrease in standard deviation will not justify.
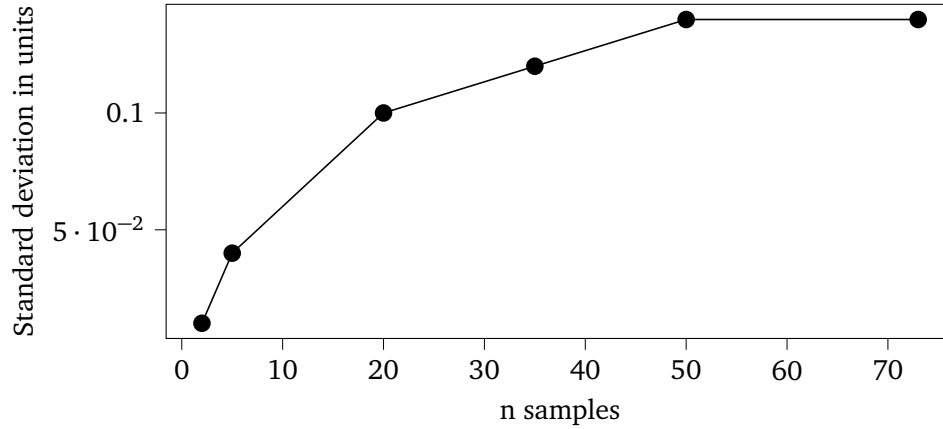
Figure 3.3: Standard deviation of the b2-component measured in units plotted against a number of coils turns.

3.2 Compensation of known errors

The measurement setup have some known errors, which in the further sections will be presented, together with the compensation done to minimize them.

3.2.1 Gap calibration and coil resistance

The rotating coil mapper's shaft consists of three coil segments, 2 outer segments, and one central segment. The central coil features a small gap, which needs to be compensated for. Here, the method for calculating it is laid out using a single-stretched wire measurement together with a rotating coil measurement of the field. Then, the effect of the coil's resistance and the resistance of the Fast-Digital Integrator is calculated and added to the compensation factor.

$$I(A_n) := \int_{-\infty}^{\infty} A_n(z)\,dz, \quad \text{and} \quad I(B_n) := \int_{-\infty}^{\infty} B_n(z)\,dz \tag{3.1}$$

is the equation for the integrated multipoles (where $I(C_n)$ means integrated, not current). For the following calculations, it's assumed that it is sufficient to only integrate between the measurement length L_{meas}. In reality, this is a good assumption since the field decays fast with distance. The integrated field-harmonics have been determined using a single-stretched wire measurement, and they will be used as a "ground truth". Here is a reminder that the z-axis in the coordinate system is "through" the magnet-aperture, or along the coil as shown in figure 3.6 is in place.
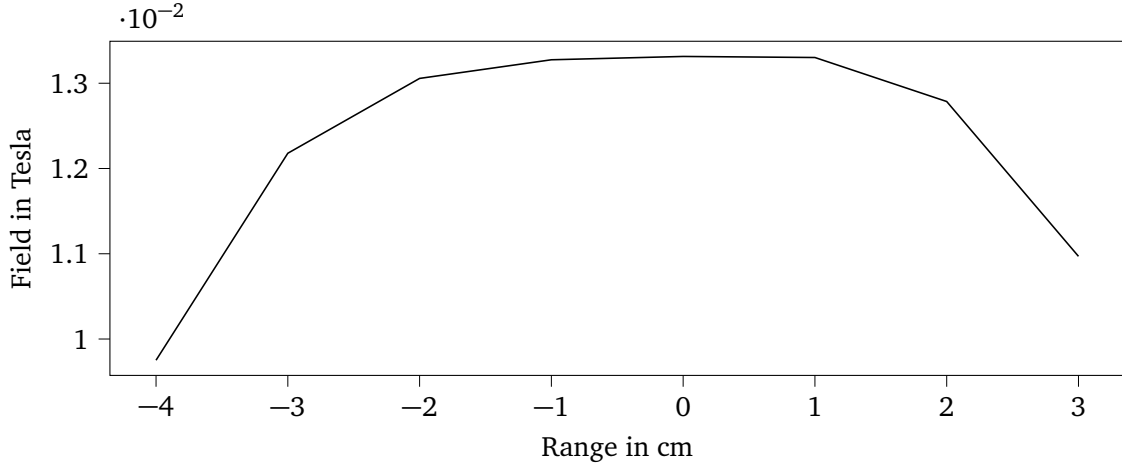
Figure 3.4: Plot of the magnetic field main component along the z-axis, showing that it is sufficiently homogenous.

The integral measurements for the field component B_1 using the rotating coil mappers coil can be expressed as

$$I_{\text{RCM}}(B_1) = \underbrace{\int_{-\infty}^{-\delta/2} B_1(z)\,\mathrm{d}z}_{=I_{\text{RCM}_{\text{seg. 1}}}(B_1)} + \underbrace{\int_{\delta/2}^{\infty} B_1(z)\,\mathrm{d}z}_{=I_{\text{RCM}_{\text{seg. 2}}}(B_1)},\tag{3.2}$$

where δ is the distance between the two integral coils, which is the unknown gap.

The field needs to be sufficiently homogeneous in the interval position $-\delta/2 \leq z \leq \delta/2$, such that the multipole $B_1(z=0)$ can be recovered from the measurements of the central coils of the RCM. From figure 3.4 one clearly sees that this is the case, as there is almost no variation of the field around the point chosen as 0 in the z-axis.

Developing the equation further then yields

$$\underbrace{\int_{-\infty}^{\infty} B_1(z)\,\mathrm{d}z}_{\text{SSW}} = \underbrace{\int_{-\infty}^{-\delta/2} B_1(z)\,\mathrm{d}z}_{\text{RCM segment 1}} + \underbrace{\delta B_1(z=0)}_{\text{RCM center}} + \underbrace{\int_{-\infty}^{-\delta/2} B_1(z)\,\mathrm{d}z}_{\text{RCM segment 2}}.$$

The descriptions in the equation above indicate which measurement system is used to determine each of the terms. Going on one obtains

$$I(B_1) = I_{\text{RCM}}(B_1) + \delta B_1(z=0).\tag{3.3}$$

The calibration coefficient δ can now be determined from

$I(B_1)\,[\mathrm{Tm}]$	$I^*_{\mathrm{RCM}}(B_1)\,[\mathrm{Tm}]$	$B^*_1(z=0)\,[\mathrm{T}]$	$I_{\mathrm{RCM}}(B_1)\,[\mathrm{Tm}]$	$B_1(z=0)\,[\mathrm{T}]$	$\delta\,[\mathrm{mm}]$
0.3372	0.3335	0.7062	0.3345	0.7064	1.38

Table 3.1: Results of the cross-calibration procedure using the SSW measurement system.

$$\delta = \frac{I(B_1) - I_{\mathrm{RCM}}(B_1)}{B_1(z=0)} \tag{3.4}$$

Table 3.1 holds the summarized results obtained from a cross-calibration with the Single-Stretched Wire system. The values marked with a * symbol are the ones obtained before correcting for the input resistance.

The gap size found is validated by measuring the mechanical gap between the PCBs with a caliper. The measured value is ~ 1.05 mm. The calibration gives a value of 1.38 mm, which is 0.32 mm larger.

Both the coils and the FDI have a resistance that needs to be compensated for. In table 3.2 the resistance of the FDI and coils is presented, together with the calculated correction factors, which the flux needs to be multiplied by to get the true value. In figure 3.5 the equivalent measurement circuit is presented.
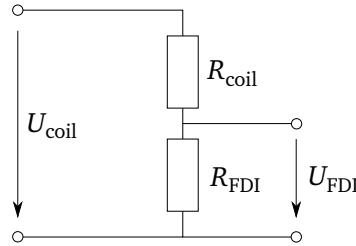
Figure 3.5: Equivalent measurement circuit is a simple voltage divider.

Coil	R_{coil} in kΩ	R_{FDI} in kΩ	correction factor
Integral absolute	2.386	400	1.00592
Center absolute	0.1134	400	1.00028
Integral compensated	4.775	400	1.0118
Center compensated	0.2263	400	1.00057

Table 3.2: Coil resistances and calibration factors.

3.2.2 Correction of earth's magnetic field

The earth's magnetic field is always present, and have an value around 25-65 μT. For the measurements, this is a systematic error, and needs to be considered. Since earth's magnetic

field essentially is constant, one can therefore take the $anti-average$ of the measurements to remove earth's magnetic field from the result. Let $B1 = b1 + m$ be an measurement with positive current, where $b1$ is the B-field from the magnet and m is earth's magnetic field, and where $-B1 = -b1 + m$ be an identical measurement with negative current. Then

$$Anti-average = \frac{(b1+m)-(-b1+m)}{2} = \frac{b1+b1+m-m}{2} = b1 \qquad (3.5)$$

This cancels out the earth's magnetic field (m) and to obtain a correct value, this procedure must be repeated for every measurement.

3.3   Measurement setup

The setup used to take the measurements is shown in figure 3.6. The stages can move the shaft around in the x-y plane inside the magnet aperture, with the motor controlling the shaft mounted directly on the stages. The shaft consists of 6 coils, two on each side of the magnet and two in the middle. The coil shaft has a radius of 31 mm and has a radial-coil configuration.
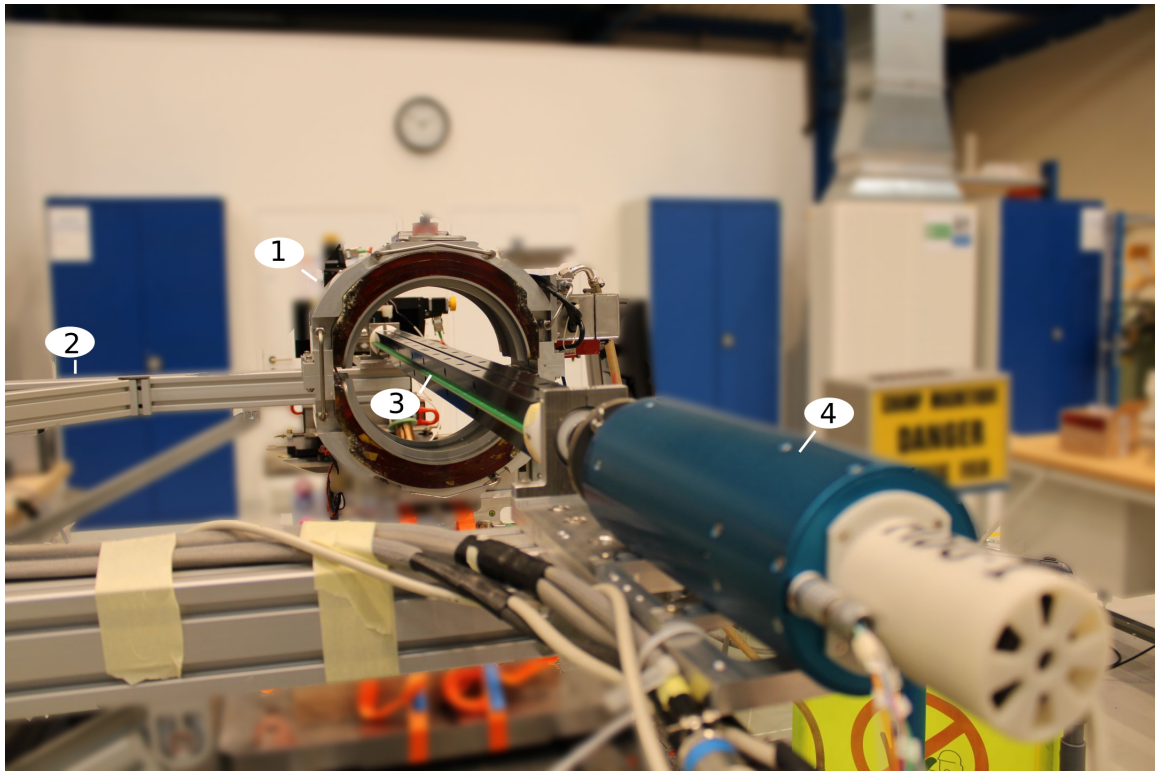
Figure 3.6: Measurement setup on the rotating coil mapper used validation of the measurement method. The image shows the magnet (1), the linear stages (2), the shaft with one of several PCB coils visible (green) (3), and the motor controlling the coil (4)

A measurement then consists of the operator choosing how many positions inside the magnetic field to measure, together with the number of multipoles N to take from each position. The coil will then move sequentially from the first position to the last, stopping at each position and rotating 20 turns while taking the flux. The average flux of the 20 turns at each position is then taken. This process is illustrated in figure 3.7.

The magnet used is an AirCoil-magnet, meaning that it does not rely on ferromagnetic materials for induction, just the current flowing in the wound coil wires. The magnet has two modes, it can be either a dipole or a quadrupole magnet. This implies that the field will be more distorted than if it was either only a dipole or quad. The magnetic aperture is large by accelerator-magnet standards, measuring 90 mm in radius (obtained by checking with a ruler),
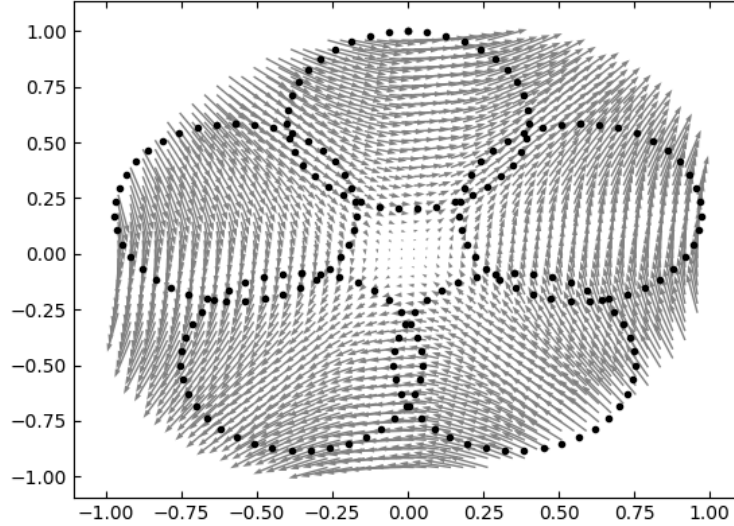
Figure 3.7: Illustration of one measurement of 5 positions (I=5) inside the magnetic field, with the grey arrows representing the magnetic field, and the black circles representing the traces of where the coil measures. The coil moves sequentially from the first position to the last.

and it also has a low magnetic field, with a maximum current of 45 A. These two attributes it must be noted would be unsuitable for most of the other standard ways of mapping the magnetic field, and thus it is a perfect match for the oversampling technique.

3.3.1   Combination of signals acquired by coil segments

As noted, the coil shaft features a small gap in the middle, together with 3 segments each consisting of two coils. This means each segment is acquiring a signal, which then needs to be combined.

Since the coil gap is calculated and known from section 3.2.1, the combination can be done according to each segment's length and impedance correction.

$$B_1 = \alpha_{1_{abs}} \cdot l_{coil} \cdot B_{1_1} + \alpha_{ctr_{abs}} \cdot l_{ctr} \cdot B_{1_{Ctr}} + \alpha_{2_{abs}} \cdot l_{coil} \cdot B_{1_2} \tag{3.6}$$
$$A_1 = \alpha_{1_{abs}} \cdot l_{coil} \cdot A_{1_1} + \alpha_{ctr_{abs}} \cdot l_{ctr} \cdot A_{1_{Ctr}} + \alpha_{2_{abs}} \cdot l_{coil} \cdot A_{1_2}$$

For the first two multipoles, the absolute value for the impedance correction is wanted, which is α, l_{coil} is the length of one of the two side-segments, and l_{ctr} is the length of the calculated center gap. Each segment measures a multipole, and this is $B_{1_{1/ctr/2}}$ which is either segment 1, the central segment or segment 2.

For the rest of the combination, the compensated (meaning they are bucked) signals are wanted, meaning that α is now α_{comb} instead.

$$B_n = \alpha_{1_{comb}} \cdot l_{coil} \cdot B_{n_1} + \alpha_{ctr_{comp}} \cdot l_{ctr} \cdot B_{n_{Ctr}} + \alpha_{2_{comb}} \cdot l_{coil} \cdot B_{n_2} \tag{3.7}$$
$$A_n = \alpha_{1_{comp}} \cdot l_{coil} \cdot A_{n_1} + \alpha_{ctr_{comb}} \cdot l_{ctr} \cdot A_{n_{Ctr}} + \alpha_{2_{comp}} \cdot l_{coil} \cdot A_{n_2}$$

3.3.2 Rotation in a common reference frame

The multipoles of each measurement position need to be expressed in a common reference frame. This is done by rotating the multipoles according to the equation

$$C_{n_{rot}} = C_n e^{-in\tau} \tag{3.8}$$

where τ is the angle. It is standard practice to find the angle that gives $A_1 = 0$. This was found by experimental validation to be -103.5 degrees for the magnet and was thus applied to all measurement positions. As seen from the factor n, a large multipole order gives a higher rotation. Since this rotation is done, the A_n multipoles have a smaller value than the B_n multipoles, and thus they can generally be neglected. This will be the case in this thesis, and the results will often be presented with just details of the B_n component. The A_n will be included in some sections, where they are large enough to not be neglected.

3.4 Establishing a reference

Due to the AirCoil magnet's large aperture, it is hard to establish a reference of the multipoles to compare the measurements to. This is needed to find a "ground truth" to characterize the measurement precision and accuracy. The most convenient way would have been to measure the whole field at once using a coil with a radius close to the magnet-aperture radius, thus obtaining essentially the whole field perfectly. Since the measurement laboratory doesn't have a coil with a large enough radius, this is an unfeasible approach.

3.4.1 Reference from rotating coil

One way of obtaining a reference to compare the measurements too is by using a normal rotating coil measurement taken in the middle of the magnet. Since the magnetic field is very low, it is expected that some of the multipoles are not measured precisely. Nevertheless, it gives an idea of the magnetic field, and it is also completely free of positioning errors. The trends should match, but the higher-order multipoles become to small to be measured at a point.

It is common to express the multipoles at a reference radius equal to $\frac{2}{3}$ of the magnet aperture, which in this case would have been 53 mm. A measurement with the normal rotating coil method would have been unable to express the multipoles at this radius, as it would simply extrapolate into an unknown area. The oversampling method can do this, as this area is actually measured. For comparison, the reconstructed multipoles will be scaled down to the same radius as the central coil.
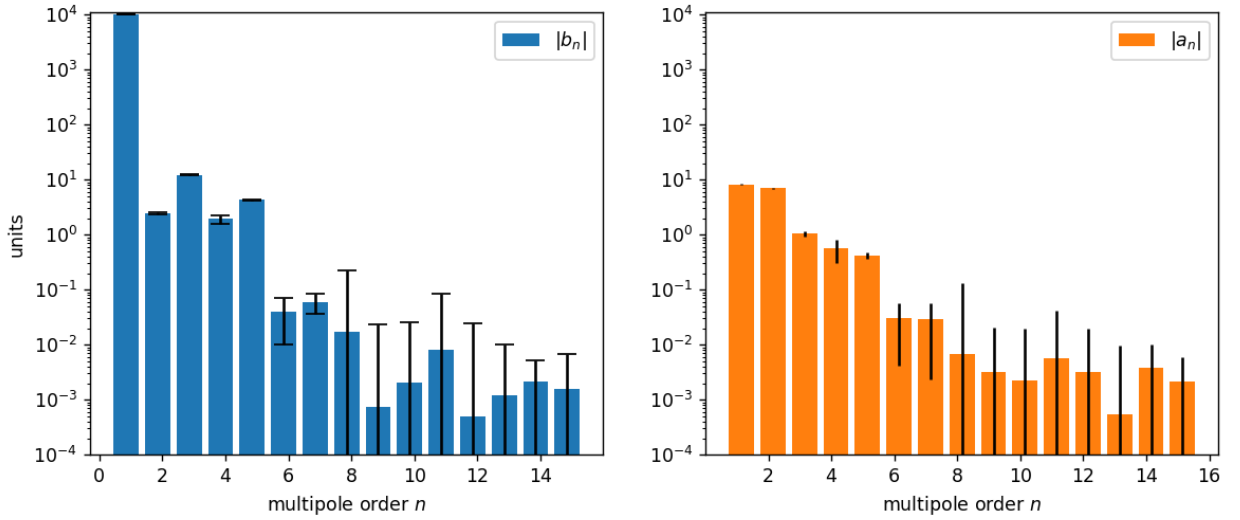
Figure 3.8: Multipoles acquired from the average of 8 central measurements, given in *units*, with 3σ overlaid in black error bars, to show the standard deviation. After multipole order, $n \approx 8$ the multipoles are indistinguishable from noise.

The reference measurement was taken in the center of the magnetic field, using a current $I = 45$ A, the standard coil having a radius $R_c = 30$ mm, and using 20 rotations. The measurement was then repeated 8 times, and the average was taken. All measurements were done with dipole-bucking, meaning the dipole-component (B_1) is bucked out to increase sensitivity for all the other harmonics. Table A.1 is showing the magnetic field B in Tesla, the normalized magnetic field b in units and the standard-deviation of the 8 measurements also given in units for each multipole order n.

From figure 3.8 it is clear to see that the higher-order multipoles are to small to be distinguished from noise, The first 5 multipoles features almost no standard-deviation for both normal and skew, and the higher-order multipoles starting from multipole order 8 features a 3σ deviation larger than the value itself, indicating they are noise. This further supports the argument made in section 2.2.3 for using the lower-order harmonics to reconstruct the higher-order harmonics.

3.4.2 Reference from Single-Stretched Wire measurements

A reference using the Single-Stretched Wire method was obtained. Since this is a different measurement method, it is also subject to different errors as the rotating coil system. It is not expected that the results match completely, but nonetheless, the trends should match. The SSW system is the method most suited for measuring a large-aperture magnet, as the method is similar, one moves the wire along a measurement radius, which can be close to the magnetic aperture.
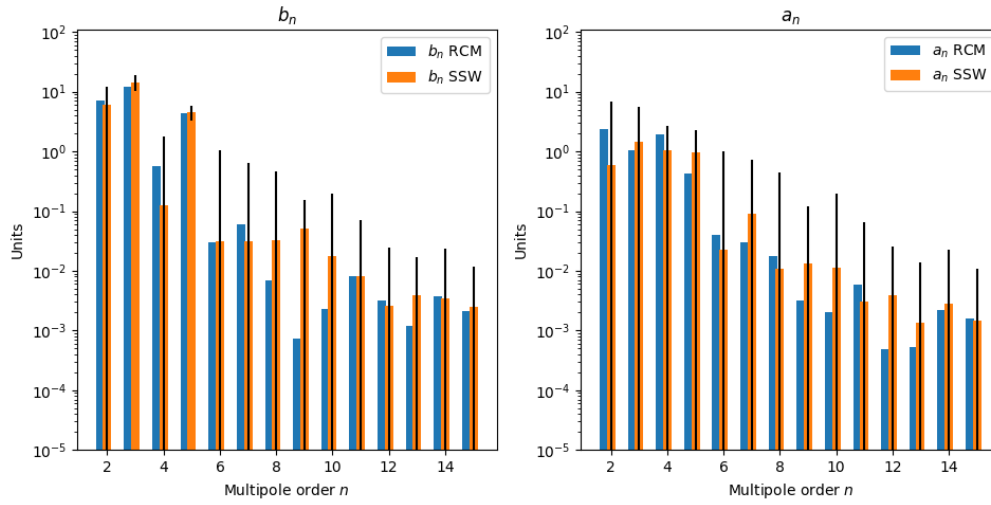
Figure 3.9: Comparison between central reference measurement and the Single-Stretched Wire measurement, SSW plotted with 3σ error overlaid.

However, it is challenging to measure a low-field magnet with the wire system. As stated in section 2.3.4 the SSW method can be viewed as a rotating coil taking one turn. Therefore the sensitivity to small fields is low, and an adequate result for the higher-order multipoles is not obtained. This could be overcome in several ways, such as taking more measurements with the wire and averaging out.

The Wire was measured at a measurement radius $r = 50$ mm, and the multipoles were then scaled down to a reference radius $r_c = 30$ mm, so they are all expressed at the same radius. An average of 3 measurements were taken, with a step size of 10 mm, meaning the wire measured a point along the circular path, moved 10mm, and measured again, repeating the process the whole way.

As is the case for the central reference obtained by the rotating coil system, the SSW measurement fails to obtain the higher-order multipoles, and after multipole order $n \approx 5$ noise is measured. The 3σ error is large and is therefore included in the plot as overlaid error bars.

Chapter 4

Results and analysis

In this chapter, the results obtained from the measurements are laid out, together with a comparison with the reference measurements. Thereafter, an analysis of how different parameters such as positions chosen and a number of multipoles used for reconstruction affect the outcome is presented. If not specified, all the results are presented in units of the main field, meaning normalization to the main field component, as discussed in section 2.2. Lastly, a measurement outside the domain of validity of the equations is presented, together with an analysis of the error which ensues.

4.1   Validation of the oversampling-technique

This section aims to validate the oversampling method, with first a look at the reconstructed multipoles compared to the central measurement obtained by the rotating coil. Afterward, a comparison between the reconstructed multipoles and the Single-Stretched Wire measurement is done. All measurements done with the rotating coil are done with dipole-bucking applied.

Since none of the references used is able to measure the higher-order multipoles precisely, the section then aims to prove that the reconstructed multipoles are valid for the higher-order multipoles by exploiting some properties of the equations, and by looking at how the standard deviation behaves.

Measurement radius

The magnet was found to have a radius of 80 mm by simply moving the coil in both the x and y direction and seeing what the spread in values was. This was done by eyesight and is not precise. By using a ruler, the magnet was found to have a radius of 90 mm. Since moving the coil into the magnet aperture would break the coil, a measurement radius of 75 mm was set as the maximum measurement radius, except for the $C_n(r)$ measurement presented later, which was slightly over this radius.

Measuring closer to the magnet aperture would obviously improve the precision by measuring a stronger field, as explained in section 2.2.3. Thus, even though the measurement radius is
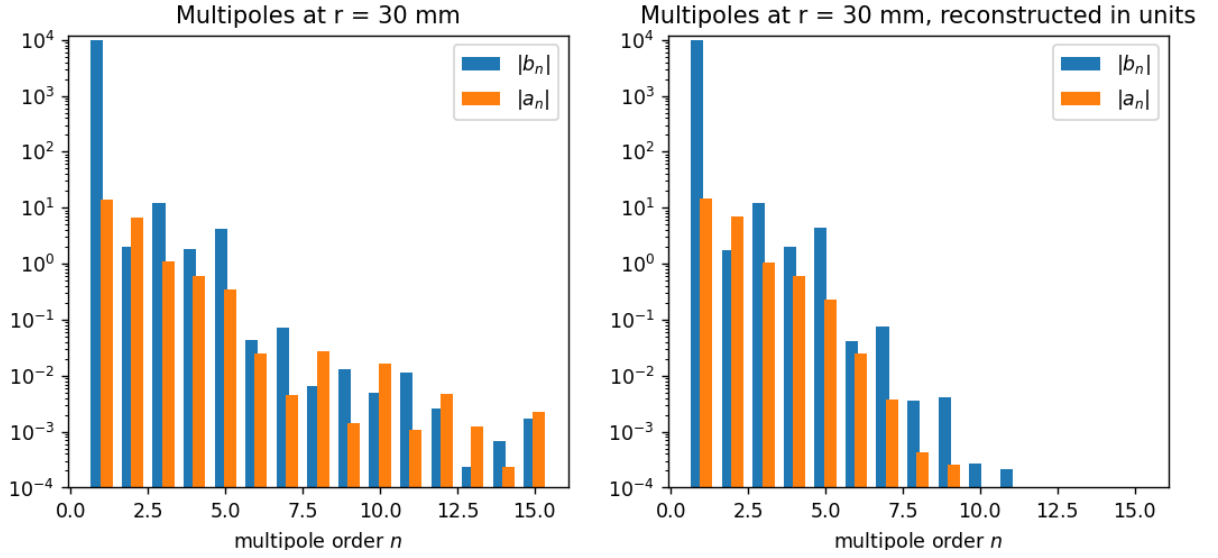
Figure 4.1: Comparison between the reference measurement to the left and the reconstructed multipoles expressed on the same reference radius $r_0 = 30mm$ to the right.

an important parameter, this thesis will not look into the effect. In the future, when a system for avoiding breaking the coil is in place in case of human error such as entering the wrong measurement radius, this effect can be studied further.

4.1.1 Comparison between reconstructed measurements and central reference

For the validation of the method, measurements consisting of 42 positions each acquiring 6 multipoles were taken, using a measurement radius of 75 mm, with a condition number $\kappa = 28$. The multipoles were then reconstructed on the same radii as the small coil, meaning $R_c = R_0 = 30$ mm. The reason to scale down the reconstruction instead of scaling up the reference taken in the middle with a single coil is to avoid scaling up any errors there might have been in the measurements.

From figure 4.1 one clearly sees that the reconstruction matches the reference measurement until multipole order $n \approx 7$. After multipole order 7, the middle measurement measures only noise, which can be seen from the multipoles "flattening" out, while the reconstructed multipoles continue decreasing logarithmically. This is discussed in section 2.2.3 , and indicates that the reconstructed multipoles are valid for higher orders than the middle measurement. Said in another way, the reconstructed multipoles are valid below the equipment's noise floor, and thus gaining precision in the higher-order multipoles.

To further validate, another reconstruction was calculated, using 14 measurement positions each acquiring 5 multipoles, reconstructing on a radius of 30 mm and having a measurement radius of 75 mm, with the same condition number $\kappa = 28$. The results from the central ref-
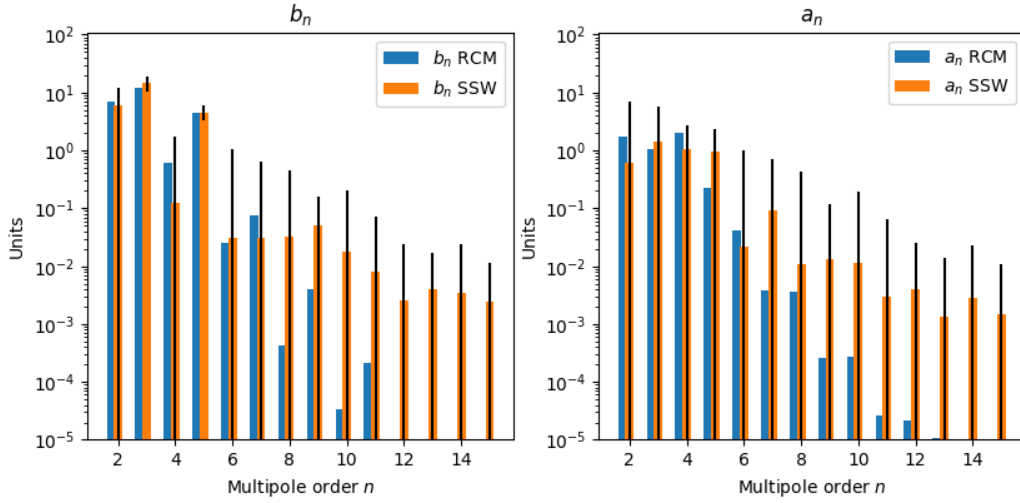
Figure 4.2: Comparison between the reconstructed multipoles with $I = 42$ positions and the Single-Stretched Wire measurement. The SSW is plotted with 3σ overlaid in black.

erence, the reconstruction using 42 positions and the reconstruction using 14 positions are presented in table A.2.

From table A.2 is it clear to see that both reconstructed values agree with the reference measurement, having less than one unit difference for all lower-order multipoles expect b_2 which corresponds to the magnetic fields quadrupole component. Both reconstructions also have valid multipoles for the higher order ones, generally flattening out and thus reconstruction noise around $n = 12$, although the reconstruction with 42 measurement positions ($I = 42$) seems to follow the trend with logarithmic decay longer, thus implying higher precision. This is to be expected as this measurement have more equations to fit.

4.1.2 Comparison between reconstructed multipoles and Single-Stretched Wire measurement

Figure 4.2 shows both the normal and skew multipole components obtained from the reconstruction (blue) and from the Single-Stretched Wire measurement (orange). As is expected, the measurements are matching for the first $n \approx 6$ multipole orders, and afterward, the SSW-measurement are only measures noise, while the oversampled multipoles continue decaying as expected.

The reconstructed measurement is always close to the 3σ deviation of the SSW measurements for the lower-order multipoles. It is clear to see from the SSW measurements 3σ that the SSW system has a low precision for this particular measurement. This clearly illustrates the challenges of measuring a low-field large-aperture magnet with the available methods.
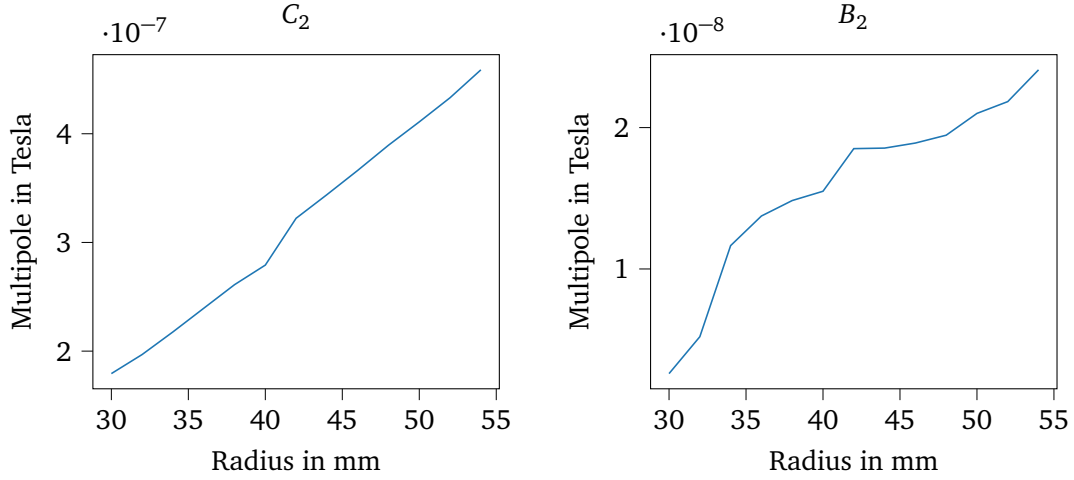
Figure 4.3: Plot of multipole order 2, both the total C_2 and the normal B_2, given in Tesla. The radius is given as the radius the linear stages moves, meaning the actual radius is the given value + the coil radius $r_c = 30mm$.

4.1.3 $C_n(r)$

As seen from the previous sections, verifying the methods using the available references is hard since both methods used to obtain the reference measurement are not well-suited for this use case, and thus no reference for the higher-order multipoles is obtained. By looking at the mathematics behind the multipole-equation, an experiment can be designed in such a way that the higher-order multipoles can be validated. As known from the equation governing the field-harmonics(equation 2.15), the multipoles grows exponentially, dictated by the term

$$C_n \left(\frac{z}{r_0} \right)^{n-1} \tag{4.1}$$

It is clear to see that by increasing the radii, thus increasing z, each multipole should grow to the power of $n-1$. Since the chosen reference measurements are unable to obtain the higher-order multipoles, one can exploit this fact to see if the reconstructed higher-order multipoles are valid. Plotting the multipole value versus range in mm gives a slope, starting from a straight line for the first component, all the way up to a polynomial with 15 degrees for the 15th harmonic. The smoothness of the slope is an easy way to illustrate whether the reconstruction is good or not. A smooth slope without bumps indicates that the reconstructed multipoles grow as expected, and an uneven slope with a lot of bumps indicates a bad reconstruction.

Measurements with different radii were taken, from a measurement radius of 50 mm, with increments of 2 mm, up to 80 mm. All measurements measured 15 multipoles, and had 14 measurement positions each. The reconstruction radii for each measurement were the same as the measurement radii. Only the C_n and B_n are plotted, as the relationship $C_n = A_n + iB_n$
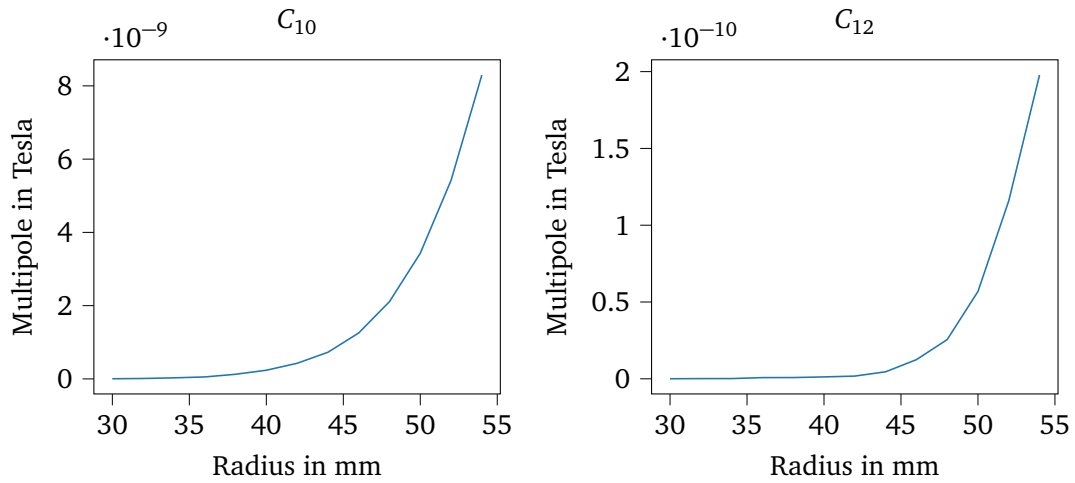
Figure 4.4: Side by side plot of C_5 and C_8 field components. The two multipole orders were chosen to illustrate by the author, but all the other reconstructed components behaved as expected. The radius is given as the radius the linear stages move, meaning the actual radius is the given value + the coil radius $r_c = 30mm$.

makes it easy to deduce the A_n from the plots, and the A_n are rotated to be zero. From figure 4.3 magnets quadrupole-component is plotted, which is the second order multipole. This is expected to grow linearly. The total harmonic C_2 grows linearly, while the normal component B_2 is uneven. Notice the order of magnitude difference in field value between the C_2 and B_2. This means that a large a_n skew component is reconstructed.

Figure 4.4 shows the field harmonic of orders 10 and 12. The multipoles are expected to grow with exponential order of 10 and 12. From the two plots it is easy to see that C_{12} grows exponentially faster than C_{10}, as expected. Both graphs are smooth, which indicates that both reconstructions are good. Here one should note that all reconstructions and their respective plots behave as expected, except for the C_2 component, which will be addressed.

4.1.4 System standard-deviation

For the standard deviation of the whole system, 8 measurements were taken using 14 measurement positions and 5 multipoles on a measurement radius of 75 mm. The reconstructed multipoles were then expressed on a radius of 30 mm. The standard deviation of the 8 measurements was then taken. 14 measurement positions were chosen as a compromise of the total time used for measuring, while still being enough positions to reconstruct the field sufficiently and having an influx of mechanical and random errors. From figure 4.5 it is clear that the improvements in precision come in the higher-order multipoles. Where the standard deviation for the harmonics higher than order 7 in the middle measurement are just noise and eventually flattens out, one can observe that this is not the case for the reconstructed multipoles.
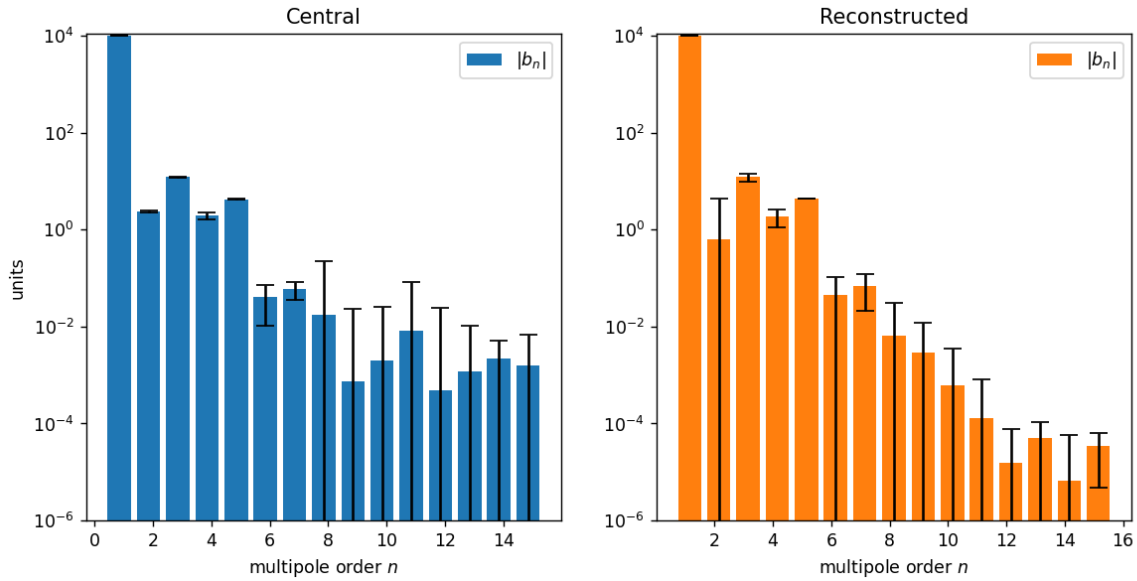
Figure 4.5: Comparison between reference measurement and the reconstructed multipoles with 3σ overlaid in black error bars.

The trend with logarithmically decaying multipoles and thus standard deviations is continuing up until multipole order 12 for the reconstructed multipoles. The b_2 component in the reconstructed multipole has a 3σ higher than the multipole value itself, and needs to be addressed.

Comparing the b_2 component in this reconstruction using 14 measurement positions, and the one using 42, it is clear that there is some unit difference in the value. As seen from section 4.1 the quadrupole component C_2 in the reconstruction doesn't match well with the reference, and this needs to be addressed. A further explanation will be given in a later section.

From table A.3 (included in the appendix) it is clear that the reconstruction has a lower standard deviation starting from multipole order 8, where it has decreased the standard deviation by 2 orders of magnitude compared to the central reference.

The standard deviation for the lower-order multipoles is better for the central measurement, which is to be expected as the positioning error of the system is the limiting factor for precision when doing the oversampling. Nonetheless, the differences in standard deviation are one order of magnitude worse, which for the lower-order multipoles means the unit range.

4.1.5 Methodical standard-deviation

Looking at the system standard deviation, as done in the way above includes mechanical errors of the system, such as the positioning error. Thus, the standard deviation is only comparable between measurements done on this particular magnet, and it is a bit of a stretch even to compare using results obtained in two different methods. Since the standard deviation affected
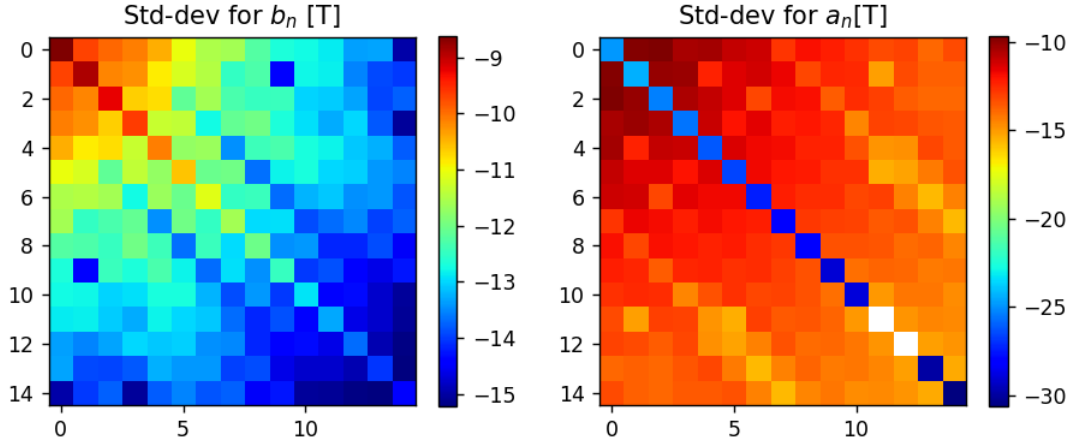
Figure 4.6: Heatmap showing square root of the covariance matrix with the standard deviation for each reconstructed multipole of the method along the diagonal. The value is given in Tesla, with the logarithm taken. $I = 14$ measurement positions.

by positioning error depends on the actual field measured, it would vary depending on the magnet used for the measurement. A magnet with a strong field gradient would be affected more in the standard deviation with a small displacement error than a magnet with a weak field gradient, and thus comparing the results is only valid on this specific magnet.

Therefore, the mechanical errors will be taken out, and this section will only look at the standard deviation coming from the method itself. This is done by using the matrix M from equation 2.29. The matrix M holds as explained before the information about the radius, measurement positions, and the binomial coefficients of the series expansions. Combining this with the standard deviation of the multipoles obtained at each measurement position called $G_{i,k}$. These multipoles C'_n are *not* expressed at a central radius and position, but the actual multipoles obtained at each coil position without any more post-processing done, and are thus independent of the positioning error. Taking

$$
\sigma'^2 = \left[M^H \begin{bmatrix} \frac{1}{G^2_{1,1}} & 0 & \cdots & 0 \\ 0 & \frac{1}{G^2_{1,2}} & \cdots & 0 \\ 0 & 0 & \ddots & 0 \\ 0 & \cdots & 0 & \frac{1}{G^2_{I,K}} \end{bmatrix} M \right]^{-1}
\tag{4.2}
$$

where the inner matrix is the standard deviation from the multipoles at each measurement position $G_{i,k}$. Looking at the resulting square matrix and taking the square root, gives the method standard deviation for each multipole C_n along the diagonal given in Tesla. The standard-deviation is starts at 10^{-9}, which is about the same as the central reference standard deviation (given in table A.3), but then quickly becomes much better for the higher order multipoles.
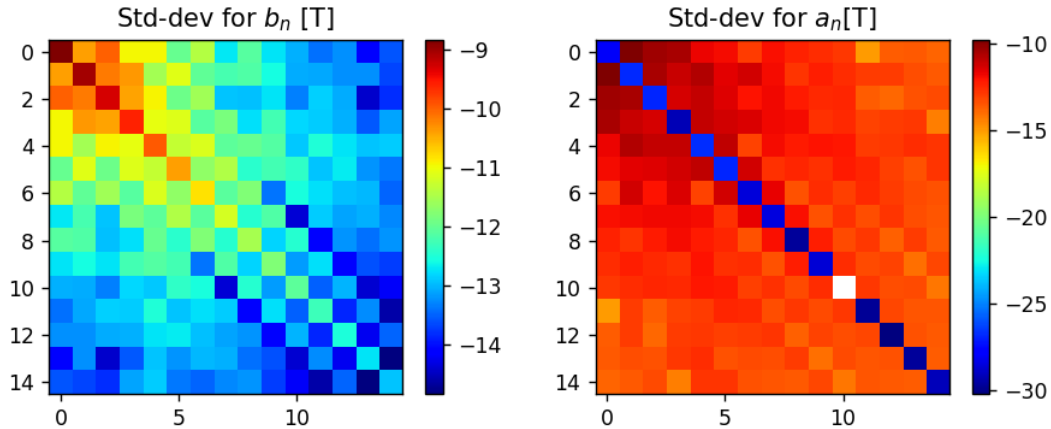
Figure 4.7: Heatmap showing square root of the covariance matrix with the standard deviation for each reconstructed multipole of the method along the diagonal. The value is given in Tesla, with the logarithm taken. $I = 42$ measurement positions.

This is to be expected as the central measurement only measures noise after multipole order 6. The values for the a_n multipoles are much lower than for the b_n multipoles. This is predictable, as they are rotated to be zero, and thus should be much lower than the b_n harmonics.

Comparing this result to the standard deviation for the reconstructed multipoles from the whole system, with the mechanical errors such as the positioning error included, the standard deviation is always 1 order of magnitude lower, and for the higher-order multipoles the standard-deviation is 3 orders of magnitude lower.

Comparing figure 4.6 ($I = 14$ positions) to figure 4.7 ($I = 42$ positions) it is clear that the increase in measurement positions lowers the standard deviation for all multipoles, as can be seen from the increased area with blue shade in the heatmap.

4.2   Analysis

In this section, a reconstruction from 42 measurement positions, using the lowest 6 multipoles to reconstruct the rest is used as a reference. The same measurements are then used for the analysis, but the parameters is changed in the post-processing of the measurements. For each section a variable is changed, and the effect is discussed.

Since the method are relying on a Least-Squares fit to find the reconstructed multipoles, the matrix $[M]$ must always be over-determined, meaning always having more than $K - 1$ equations, meaning the parameters I and N must adhere to

$$(N - 1)I > K - 1 \tag{4.3}$$

The reference used to compare with is the reconstruction using 42 measurement positions and the 5 first multipoles from each measurement position. The reference radius is 30 mm, and all the values are given in units.

4.2.1   Measurement positions

Starting from equation 4.3 it is clear that the lowest number of positions one can acquire while still using the 5 first multipoles $N = 5$ to reconstruct 15 multipoles $K = 15$ is 4. This gives us 16 equations for 15 unknowns.

The number of positions was chosen to always be a multiple of 4, leaving us with 16 positions, giving 64 equations, 32 positions giving 128 equations, and the reference reconstruction of 42 positions having 168 equations to use in the Least-Squares fit. All measurements were done a radius of 75 mm and each measurement position acquired 5 multipoles.

From figure 4.8 it is clear to see that the reconstruction using 4 measurement positions is off by at least 1 order of magnitude for almost all multipoles except the 5th harmonic. For the higher-order multipoles which have to be reconstructed using the least-squares fit, all values are wrong.

For the other reconstructions, it is clear to see that increasing measurement positions always give a result closer to the reference, but the largest gain in precision is from 4 to 16 positions, and afterward, the increase in precision is a lot smaller, but nonetheless never an exact match with the reference. Table A.4 with the exact values for the reconstructed multipoles are attached in the Appendix.

This implies that the most gain in precision comes from increasing the measurement positions when having around the same number of equations as multipoles to reconstruct, thus having just enough equations for the system to be over-determined. The relationship of precision gained vs measurement positions is not linear, so simply doubling the number of equations for the fit is not giving double precision.

Increasing measurement positions by a factor of 4 from 4 to 16, increases the equations for the reconstruction from 16 to 64. For the lower-order multipoles the reconstruction using 16
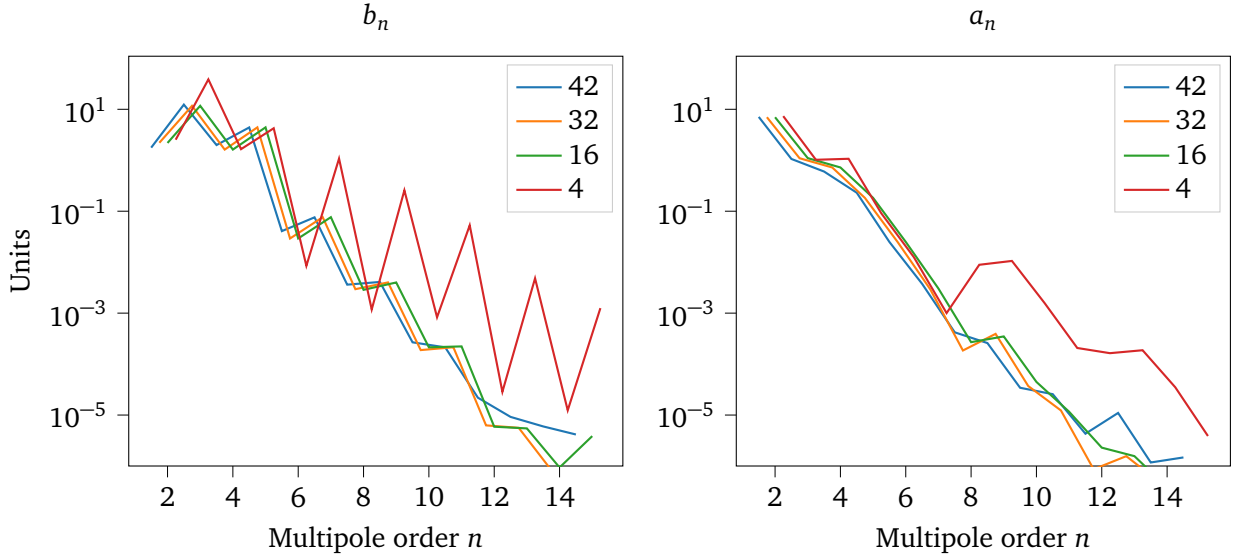
Figure 4.8: Plot of the different reconstructions using $I = 42$, $I = 32$, $I = 16$ and $I = 4$ measurement positions, and $N = 5$ multipoles used for reconstruction to reconstruct all the $K = 15$ multipoles. Each graph is shifted slightly along the x-axis, making it more clear to see the plots.

positions agrees quite closely, and it is first around multipole order $n = 12$ that the reconstructions using $I = 16$ and $I = 32$ differ noticeably from the reference. From table A.4 the same trend appears, and the reconstruction has the same order of magnitude up until $n = 12$.

4.2.2 Robustness of multipole reconstruction

The difference in the b_2 component for the reconstructions having $I = 42$ and $I = 14$, together with the large difference in standard deviation, while the other multipole orders match quite well gives a clue into a weakness of the method.

One can expect that for some combinations of the physical parameters; coil size, measurement radius, and measurement positions one can have high or large sensitivities to some multipoles. This looks to be the case for this particular case for the second-order harmonics, which corresponds to the quadrupole component. To verify this, the matrix M from equation 2.28 can be used.

Using

$$Q = \left[M^H \cdot M \right]^{-1} \tag{4.4}$$

where H is the Hermitian operator (which is the transpose matrix operator for a complex-valued matrix). If now looking at the diagonal entries of the matrix, this corresponds to the
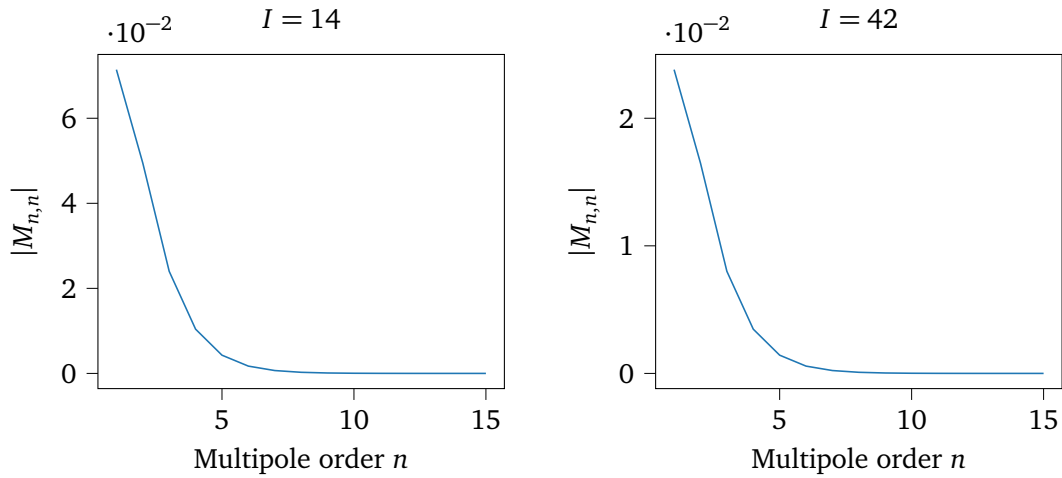
Figure 4.9: Plot of the diagonal entries from the matrix $\left[M^H \cdot M\right]^{-1}$ with $I = 14$ and $I = 42$ measurement positions. Both plots have $r_c = 30 \ mm$ and $R_m = 75 \ mm$, where R_m is the measurement radius

robustness of the multipole reconstruction, where $Q_{0,0} = C_1$, $Q_{1,1} = C_2$, and so forth. The higher the number, the more sensitive the particular multipole order is to noise and random errors. The two plots in figure 4.9 are with $I = 14$ and $I = 42$ measurement positions. Comparing the two plots it is clear that increasing the number of positions gives more robustness to the reconstruction, as is to be expected.

Figure 4.10 have the exact same parameters as the leftwards plot in figure 4.9, expect that the measurement radius R_m is increased by 30 mm, from 75 mm to 105 mm. As can be seen, the two plots are almost identical, only showing a slight effect in the first two multipoles. This suggests that the number of measurement positions has more influx on the robustness of the multipole reconstruction than the measurement radius.

$\cdot 10^{-2}$

$$I = 14, R_m = 75mm$$
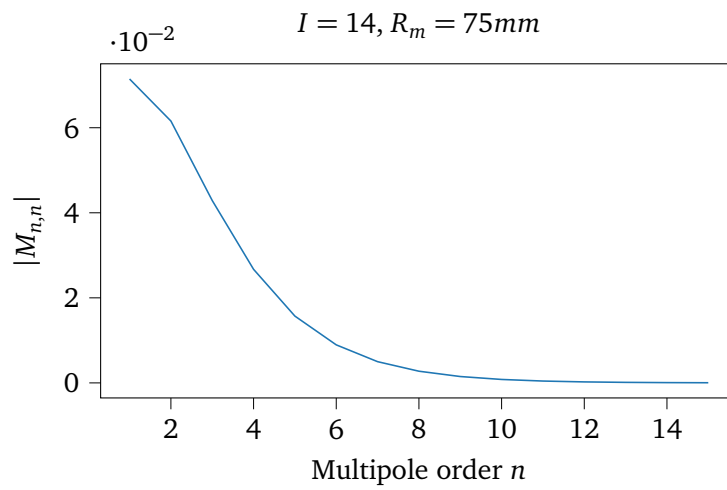
Figure 4.10: Plot of the diagonal entries from the matrix $\left[M^H \cdot M \right]^{-1}$ for $I = 14$ and measurement radius $R_m = 105 \ mm$.

4.3   Reconstruction outside the validity-domain
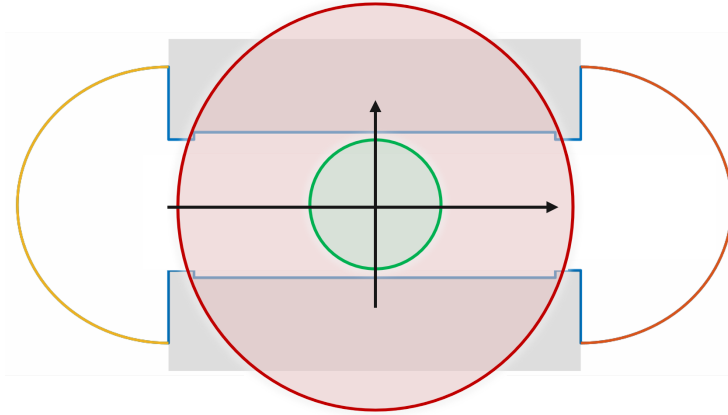
Figure 4.11: Illustration of the magnet with the fringe fields in yellow and orange, the valid reconstruction radius in green, and the reconstructed field in red(not valid). The grey area is the magnet aperture, which is *not* free of charge.

Since the multipole-equation (equation 2.15 is a complex power series, the Cauchy-Hadamard [1] theorem states that the series has a radius of convergence. This essentially means that the power series only converge on a circular domain, and trying to express the multipoles outside of this domain means they do not converge. As stated in section 2.2 one cannot extend this circle further than the magnetic aperture, thus breaking the condition that the magnetic field being mapped must be free of charge

$$\nabla \times B \neq 0 \tag{4.5}$$

Nevertheless, a measurement and subsequent reconstruction of the multipoles on a magnet with such an aperture geometry that it forces the circle to be extended outside the validity domain will be presented, together with an analysis of the results. It must be stressed that this is mathematically not allowed, and the equations are expected to break down.

4.3.1   Measurement setup

The magnetic aperture measures 60 *mm* in the y-direction and 180 *mm* in the x-direction. This obviously means that all reconstructions including x-positions with a radius of more than 30mm should break down since the radius of the circle then will extend into the magnetic aperture. This is illustrated in figure 4.11.

The magnet is shown in figure 4.12 and is a dipole magnet with the field going from the top-bottom of the magnet. The coil used had a diameter of 37 *mm*, and a current of 500 *A* was applied and kept static. The coil was then moved subsequently in the x-direction. Setting x=0 in the coordinate system as the middle of the magnetic x-axis, measured in increments

---

[1]https://en.wikipedia.org/wiki/Cauchy-Hadamard_theorem, visited January 2023

Figure 4.12: The setup of the dipole-magnet, is identical to the setup of the AirCoil-magnet, except for the magnet itself.

of 10 mm, starting from -90 mm up to $+90$ mm. The y-position of the coil was kept static, at $y = 0$ meaning the middle of the top and bottom of the magnetic aperture.

4.3.2 Field mapping outside validity-domain

The reconstruction was done with a radius of 90mm, thus representing the red circle from figure 4.11. To compare, the logarithmic relative error of the field from the reconstruction and the field from 4 measurement positions were taken. The 4 measurement positions were chosen to be -90 mm, -30 mm, 30 mm, and 90 mm thus spanning the whole field in the x-direction. When looking at raw fields, one can tolerate errors on the scale of 10^{-4} T, meaning a relative logarithmic error of -4 is considered good.
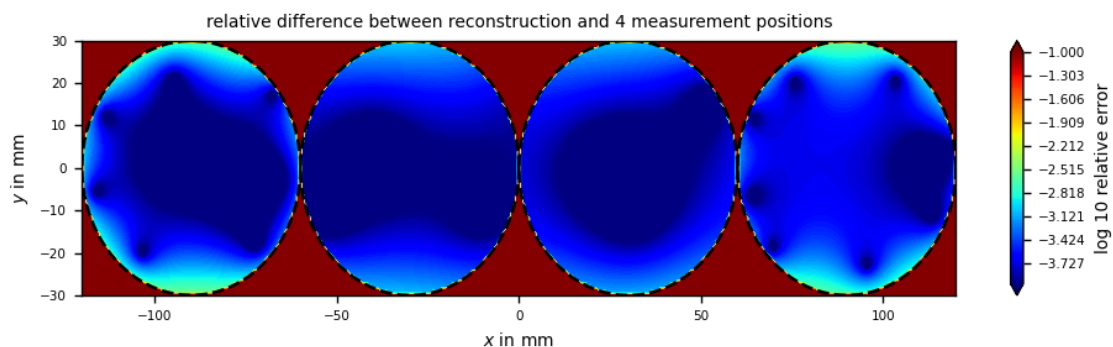
Figure 4.13: Plot showing a heat map of the relative difference between 4 measured positions and a reconstruction consisting of 19 measurements. The reconstruction radius is 90 mm.

For the first oversampling, shown in figure 4.13, 19 measurements along the x-axis, of which each acquires 8 multipoles are used for the reconstruction. The plot then shows the relative logarithmic error of the reconstructed field, compared to the actual measured field in the 4 positions. It is clear to see that with 19 measurements the relative logarithmic error is on the scale of -4.2 to -2.7. Figure 4.14 shows the effect of decreasing the positions used in the re-
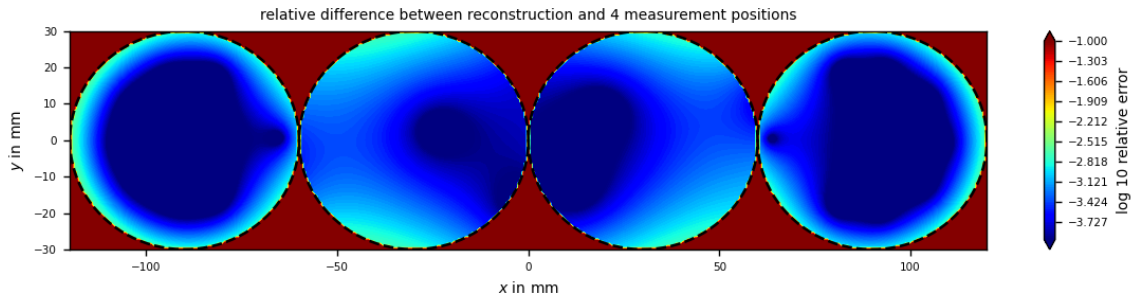
Figure 4.14: Plot showing a heat map of the relative difference between 4 measured positions and a reconstruction consisting of 3 measurements at $-90\ mm$, $0\ mm$, and $90\ mm$. Reconstruction radius 90mm.

construction to only 3, taken at $-90\ mm$, $0\ mm$ and $-90\ mm$ each acquiring 8 multipoles. It's clear to see that the area of relative logarithmic error increases, but the absolute value stays about the same.

From the measurement with 19 positions, one can see that the reconstructed multipoles and the actual measurements have a low relative logarithmic error in the center of the field (the deep blue shade), but the error quickly rises when moving out of the center. The reconstructed field have the largest relative logarithmic error in the edges, which is to be expected as this is far out of the validity domain.

For the reconstruction with 3 measurement positions, the trend is the same. The reconstruction is best for the areas directly measured by the coil. The area with a higher logarithmic error is larger, although the max value of the error stays around the same value.
Comparing the two reconstructions, it is clear to see that the reconstruction is best in the areas measured directly by the coil for both. The relative logarithmic error is close to -4 in the areas where the coil has measured directly (the areas with deep blue shade), but the error quickly falls to around -2.5 once in the reconstructed field.

This shows that the method is robust, and could be used for magnets with aperture geometries unsuited for the circular-multipole approach, depending on the requirements for precision. As long as one only takes values from the sampled areas, it is possible to reconstruct the field with a relative logarithmic error on the scale $[-4, -2.5]$. By changing the mathematical approach of the multipole equation (equation 2.15) away from being bound by convergence on a circular domain, the oversampling method would be improved. It would then be possible to measure all aperture geometries with a rotating coil system.

Chapter 5

Conclusion

The main goal of this thesis was to validate the oversampling technique for mapping magnetic fields using a rotating coil system and study the measurement impact by different tunable parameters. This was done by mathematical exploitation of the matrix properties, experimental validation, and isolating certain parameters to see what influx they had on the results.

The magnet used had a large aperture together with a low field, thus making it the typical case for the oversampling method. Measuring this magnet with conventional methods would have posed a hard problem. The oversampling technique is particularly well-suited to measuring large-aperture magnets with low fields, as seen from the failure to obtain reference measurements for the higher-order multipoles to compare the reconstructed multipoles. Validating the method on this particular magnet has shown the added strengths and flexibility of the method.

The oversampling method increases the flexibility of rotating-coil measurements, and it is now easier to measure magnets which in the past would have been unsuitable for rotating-coil measurements, which in turn helps the magnetic measurement laboratory to save cost and time by cutting down the need to manufacture specialized coils.

Using the oversampling technique to measure a low field and the large-aperture magnet has never, to the knowledge of the author, been done before and thus the results presented here are a first of its kind. The system has proved itself to be precise and has a low standard deviation, thus greatly increasing the flexibility of the rotating-coil method.

The measurement gives insight into both the strengths and weaknesses of the method. By only using the multipoles the coil can measure with sufficient precision for the reconstruction, it is possible to reconstruct valid multipoles below the precision limit of a normal rotating coil measurement, and also measure multipoles with much better precision, as seen by the calculated standard deviation which was up to 3 orders of magnitude better.

A sufficient number of measurement positions is needed to overcome the positioning error of the coil, which gives a relatively large error compared to the positioning-free error. The standard deviation free of the positioning error showed that the method has more potential, but the gains in precision will most likely be offset by the gains in added complexity by improving the positioning error.

Two sets of results were presented. From looking only at the mathematical properties of the matrices it was found that to minimize error propagation one should aim to keep the condition number low, and this was done by having a sufficient number of multipoles captured N and measurement positions I.

By looking at the matrix properties, one could determine the robustness of the multipole reconstruction for order n. By increasing the number of positions, the error of reconstruction were kept low, and increasing the measurement radius yielded only a slight improvement, implying that the number of positions I are more important than the measurement radius r_m.

The other set of results was found by experimental validation, and it was proven optimal to only use the lower-order multipoles acquired with satisfactory precision from the small coil. For this particular system, it was found that having 4 times as many equations as multipoles to reconstruct yielded a reconstruction with the same trend as the reference, and good precision. It has not been verified if this result is valid for other magnets.

The thesis ends with a reconstruction outside of the validity domain of the multipole-equation. Using the method as-is outside the validity domain with some caution is feasible, but improvements to make it more precise should be done. The measurement presented for the reconstruction outside the validity domain did inspire the development of a new mathematical basis for the multipole theory, which is free of the circular convergence condition the classical multipoles have. The combination of this new multipole theory and the oversampling-technique presented in this thesis have great future potential.

Bibliography

[1] E. of Mathematicsh. 'Analytic functions.' (), [Online]. Available: `https://encyclopediaofmath.org/wiki/Analytic_function#Analytic_functions_of_one_complex_variable`. (accessed: 29.03.2022).

[2] G. Aad *et al.*, 'Observation of a new particle in the search for the Standard Model Higgs boson with the ATLAS detector at the LHC,' *Phys. Lett. B*, vol. 716, pp. 1–29, 2012. DOI: `10.1016/j.physletb.2012.08.020`. arXiv: `1207.7214 [hep-ex]`.

[3] G. Fidecaro, 'The Discoveries of Rare Pion Decays at the CERN Synchrocyclotron,' *Adv. Ser. Dir. High Energy Phys.*, vol. 23, pp. 397–414, 2015. DOI: `10.1142/9789814644150_0016`. [Online]. Available: `https://cds.cern.ch/record/2103305`.

[4] CERN. 'Cern accelerator complex.' (), [Online]. Available: `https://home.cern/science/accelerators/accelerator-complex`. (accessed: 9.01.2023).

[5] A. Einstein, 'Über einen die erzeugung und verwandlung des lichtes betreffenden heuristischen gesichtspunkt,' *Annalen der Physik*, no. 17, p. 3, 1905.

[6] O. Kostel, 'Combining rotating-coil measurements of large-aperture accelerator magnets,' p. 123, 2016.

[7] Wikimedia. 'Lorentz force.' (), [Online]. Available: `https://commons.wikimedia.org/wiki/File:Lorentz_force.svg`. (accessed: 26.01.2023).

[8] CERN. 'Radiofrequency-cavities.' (), [Online]. Available: `https://home.cern/science/engineering/accelerating-radiofrequency-cavities`. (accessed: 9.01.2023).

[9] S. Russenschuck, *Field Computations for Accelerator Magnets*. Wiley-VCH, 2011, ISBN: 978-3-527-40769-9.

[10] E. Todesco, 'Multipolar expansion of magnetic field,' p. 12, 2021.

[11] A. k Jain, 'Basic theory of magnets,' *CERN Accelerator School*, pp. 1–21, 1997.

[12] C. Shannon, 'Communication in the presence of noise,' *Proceedings of the IRE*, no. 37, pp. 12–13, 1949.

[13] C. Petrone, 'Wire methods for measuring field harmonics, gradients and magnetix axes in accelerator magnets,' p. 155, 2013.

[14] M. Buzio, 'Fabrication and calibration of search coils,' *CERN Accelerator School*, no. 1, pp. 387–422, 2011.

[15] E. Dalane, 'Magnetic measurements of the higher-order corrector magnets for the high-luminosity upgrade of the large hadron collidor at cern,' p. 178, 2022.

[16] O. Dunkel. 'A rotating coil array in mono-bloc printed circuit technology for small scale harmonic measurements.' (), [Online]. Available: `https://public.cells.es/workshops/immw17.cells.es/presentations/Tue01-IMMW17-ODunkel.pdf`. (accessed: 9.01.2023).

[17] H. Braun, 'Small-diameter rotating coils for field quality measurements in quadrupole magnets,' *20th IMEKO TC4 International Symposium*, pp. 3–4, 2014.

[18] P. Virtanen, R. Gommers, T. E. Oliphant, M. Haberland, T. Reddy, D. Cournapeau, E. Burovski, P. Peterson, W. Weckesser, J. Bright, S. J. van der Walt, M. Brett, J. Wilson, K. J. Millman, N. Mayorov, A. R. J. Nelson, E. Jones, R. Kern, E. Larson, C. J. Carey, İ. Polat, Y. Feng, E. W. Moore, J. VanderPlas, D. Laxalde, J. Perktold, R. Cimrman, I. Henriksen, E. A. Quintero, C. R. Harris, A. M. Archibald, A. H. Ribeiro, F. Pedregosa, P. van Mulbregt and SciPy 1.0 Contributors, 'SciPy 1.0: Fundamental Algorithms for Scientific Computing in Python,' *Nature Methods*, vol. 17, pp. 261–272, 2020. DOI: `10.1038/s41592-019-0686-2`.

[19] P. Rogacki, *A contribution to the development and characerization of rotating-coil magnetometers*. Shaker Verlag, 2022, p. 8, ISBN: 978-3-8440-8493-1.

Appendix A

Appendix

A.1   Tables

n	B_n	A_n	b_n	a_n	Std-dev b_n	Std-dev a_n
1	0.000225	1.85E-07	10000	8.236585	0	0.063906
2	-5.4E-08	1.57E-07	-2.41315	6.979909	0.034721	0.078091
3	-2.8E-07	2.37E-08	-12.268	1.051995	0.058204	0.040889
4	-4.4E-08	-1.3E-08	-1.93961	-0.55993	0.11162	0.084942
5	-9.6E-08	-9.6E-09	-4.28365	-0.42518	0.012634	0.0188
6	-9.2E-10	6.88E-10	-0.04073	0.030583	0.010163	0.008807
7	-1.3E-09	-6.7E-10	-0.05963	-0.0298	0.007833	0.009154
8	3.96E-10	1.54E-10	0.017578	0.006838	0.068515	0.041876
9	-1.6E-11	-7.1E-11	-0.00073	-0.00314	0.007601	0.005757
10	-4.6E-11	5.1E-11	-0.00204	0.002264	0.008011	0.0058
11	1.83E-10	1.3E-10	0.008127	0.005759	0.025008	0.012288
12	-1.1E-11	-7.1E-11	-0.00049	-0.00315	0.007891	0.005516
13	2.72E-11	-1.2E-11	0.001211	-0.00054	0.003021	0.003052
14	-4.9E-11	-8.4E-11	-0.00219	-0.00374	0.000996	0.002171
15	3.57E-11	-4.8E-11	0.001588	-0.00214	0.001782	0.001245

Table A.1: Table showing the reference measurement, from left to right, the normal(B_n) and skew(A_n) magnetic field B in Tesla, the normal(b_n) and skew(a_n) normalized magnetic field in units, and the standard deviation(σ) of the normal and skew in units, for each multipole order n

n	b_n **reference**	b_n **I=42**	b_n **I=14**
2	-2.413147	-1.767966	-0.641257
3	-12.268026	-12.362291	-12.190932
4	-1.939612	-1.988388	-1.863470
5	-4.283654	-4.398493	-4.433682
6	-0.040729	-0.040694	-0.045459
7	-0.059634	-0.075810	-0.070602
8	0.017578	-0.003621	-0.006641
9	-0.000727	-0.004091	-0.002878
10	-0.002044	-0.000267	-0.000602
11	0.008127	-0.000213	-0.000129
12	-0.000489	-0.000022	-0.000015
13	0.001211	-0.000009	-0.000051
14	-0.002194	0.000006	0.000007
15	0.001588	-0.000004	0.000034

Table A.2: Comparison between b_n values for the central reference measurement, and the reconstructed multipoles with different number of measurement positions I, namely $I = 42$ and $I = 14$. All values are given in units.

n	b_n [Units]	Std-dev middle [Units]	Std-dev recon [Units]	Std middle [Tesla]	Std recon[Tesla]
2	-2.41315	0.03472	1.23726	7.81E-10	2.78E-08
3	-12.26803	0.05820	0.78250	1.31E-09	1.76E-08
4	-1.93961	0.11162	0.25433	2.51E-09	5.72E-09
5	-4.28365	0.01263	0.02568	2.84E-10	5.78E-10
6	-0.04073	0.01016	0.01947	2.29E-10	4.38E-10
7	-0.05963	0.00783	0.01662	1.76E-10	3.74E-10
8	0.01758	0.06852	0.00813	1.54E-09	1.83E-10
9	-0.00073	0.00760	0.00312	1.71E-10	7.02E-11
10	-0.00204	0.00801	0.00098	1.80E-10	2.21E-11
11	0.00813	0.02501	0.00023	5.63E-10	5.25E-12
12	-0.00049	0.00789	0.00002	1.78E-10	4.73E-13
13	0.00121	0.00302	0.00002	6.80E-11	4.14E-13
14	-0.00219	0.00100	0.00002	2.24E-11	3.89E-13
15	0.00159	0.00178	0.00001	4.01E-11	2.21E-13

Table A.3: Table showing the numerical values for the multipoles in units, the standard-deviation of the central measurement and the standard-deviation of the reconstructed multipoles, together with the difference in units.

	42		32		16		4	
n	b	a	b	a	b	a	b	a
2	-1.76797	7.087356	-2.205	6.992716	-2.1858	6.981015	-2.52971	7.342483
3	-12.3623	1.060146	-11.7004	1.095464	-11.7057	1.101527	-38.6039	1.021095
4	-1.98839	-0.60033	-1.61917	-0.72184	-1.61996	-0.72189	-1.65096	-1.06883
5	-4.39849	-0.23066	-4.42011	-0.18228	-4.42004	-0.18306	4.242649	0.091353
6	-0.04069	0.024906	-0.02916	0.024944	-0.02921	0.025006	-0.00848	-0.01249
7	-0.07581	-0.00377	-0.0764	-0.00294	-0.07639	-0.00304	1.078871	0.001002
8	-0.00362	0.00042	-0.00295	-0.00018	-0.00286	-0.00027	-0.00118	0.008887
9	-0.00409	-0.00026	-0.00401	-0.00039	-0.004	-0.00035	-0.257	-0.01057
10	-0.00027	3.43E-05	-0.00019	3.71E-05	-0.00021	4.47E-05	-0.00083	0.001576
11	-0.00021	-2.6E-05	-0.00021	-1.2E-05	-0.00022	-1.2E-05	-0.05284	-0.00021
12	-2.2E-05	-4.3E-06	-6.3E-06	8.63E-07	-5.9E-06	2.29E-06	-2.9E-05	-0.00016
13	-9.2E-06	-1.1E-05	-5.6E-06	-1.6E-06	-5.5E-06	-1.6E-06	0.004815	0.000187
14	5.98E-06	1.17E-06	8.27E-07	4.91E-07	9.35E-07	3.8E-07	1.24E-05	-3.5E-05
15	-4.2E-06	-1.5E-06	-2.4E-07	-1.1E-08	-3.9E-06	-1.4E-08	0.001254	3.88E-06

Table A.4: Table showing the reconstructed multipoles for $I = 42$, $I = 32$, $I = 16$ and $I = 4$.

A.2   Python code

```python
import numpy as np
import matplotlib.pyplot as plt
import matplotlib.patches as patches
from scipy.special import binom
import math

## Parameters for creation of meshgrid
N=2 #This corresponds to the n-pole of a magnet, thus 1 = dipole, 2 = quad
offsetAngle = 0
amplitude = 1
Rmag = 1
scl = 6.5
## Creates rectangular mesh;
numPoints = 50
x_mesh,y_mesh = np.meshgrid(np.linspace(-1,1,numPoints), np.linspace(-1,1,numPoints))
r = np.sqrt(np.power(x_mesh,2) + np.power(y_mesh,2))
x_mesh = x_mesh[r<=Rmag]
y_mesh = y_mesh[r<=Rmag]


#--------------------------#
#        Functions         #
#--------------------------#
#Creates a vector given a point (x, y), in the case of meshgrid creates whole field
def nPoleComponent(n,x,y,amplitude, angle,Rref = 1,*, add_multipoles = False ):
    #Complex plane
    z = x+y*1j
    #Complex coefficients
    Cn = amplitude*(1+0*1j)
    #Creating By + iBy
    ByBx = Cn*np.power(z/Rref,n-1)
    if add_multipoles: #This options add simulated multipoles to the field
        for b in range(N,15,1):
            ByBx += (0.9)**(0.9*b)*Cn*np.power(z/Rref,b-N)
    #Rotation
    ByBx = ByBx*np.exp(n*angle*1j)
    #Returning By and Bx
    return(ByBx.real, ByBx.imag)

#Returns all the points of the rand of a circle
def pointsOfCircle(x1,y1,r,stepsize):
    out_x = r*np.sin(np.linspace(0,2*np.pi,stepsize)) + x1
    out_y = r*np.cos(np.linspace(0,2*np.pi,stepsize)) + y1
    return(out_x, out_y)



#Returns the B_r array
def B_r(x,y,Bx,By):
    phi = np.arctan2(y,x)
    B_r = np.empty_like(Bx)
    for n in range(len(Bx)):
        B_r[n] = Bx[n]*np.cos(phi[n]) + By[n]*np.sin(phi[n])
    return B_r

#Function used to create several circles to "measure" from
```

```python
def CircleOfCircles(x_point,y_point,r_large,r_small,stepsize,n_circles):
    if n_circles <= 1:
        (out_x,out_y) = pointsOfCircle(x_point,y_point,r_large,stepsize)
        out_pos = 1j*x_point+y_point
        overlap = 0
    else:
        (x,y) = pointsOfCircle(0,0,(1-r_small),n_circles + 1)
        d = np.sqrt((x[1]-x[0])**2+(y[1]-y[0])**2)
        overlap = r_small-d
        out_x = np.zeros(0)
        out_y = np.zeros(0)
        out_pos = np.zeros(0)
        for n in range(len(x)-1):
            out_x = np.append(out_x,pointsOfCircle(x[n], y[n], r_small, stepsize)[0])
            out_y = np.append(out_y,pointsOfCircle(x[n], y[n], r_small, stepsize)[1])
            out_pos = np.append(out_pos, 1j*x[n]+y[n])
    return out_x, out_y, out_pos, overlap

# Under follows the functions for combining several measurements
# as explained in "Combining rotating coil measurements"

#Make matrix Wi
def matrixWi(N,K,zi,r0,rc):
    result = np.zeros((N,K))*1j
    for n in range(1,N+1):
        for k in range(n,K+1):
            result[n-1,k-1] = binom(k-1,k-n)*pow((zi/r0),(k-n))*pow((rc/r0),(n-1))
    return result

#this function computes one whole matrix M
def MatrixM(N,K,r0,rc,z_pos):
    #number of positions
    I = z_pos.shape[0]
    #allocate space for matrix M
    M = np.zeros((I*N,K))*1j
    for i,zi in enumerate(z_pos):
        matrix = matrixWi(N,K,zi,r0,rc)
        M[i*N:(i+1)*N,:] = matrix
    return M

def MatrixC(t,num_circles):
    out = np.zeros(0)
    for x in range(0, num_circles):
        sp = np.fft.fft((t[(num_samples)*x:(num_samples)*x+(num_samples)]))
        out = np.append(out,sp)
    return out


#-------------------------#
# PLOTTING MAGNETIC FIELD  #
#-------------------------#

#Circle paramters
x_point = 0.0
y_point = 0.0
circle_r = 0.3
large_circle_r = 0.45
number_circles = 14
num_samples = 60 #We want the 15 first multipoles and due to Nyquist-Shannon theorem 30 samples should be enough
```

```python
#Calling function to get the field
(By_whole, Bx_whole) = nPoleComponent(N,x_mesh,y_mesh,amplitude,offsetAngle,1, add_multipoles=False)

#Next lines create circle coordinates and calculate the vectors along the rand of circles
(X,Y, pos, overlap1) = CircleOfCircles(x_point,y_point,large_circle_r,circle_r,num_samples,number_circles)
(By1, Bx1) = nPoleComponent(N,X,Y,amplitude,offsetAngle,large_circle_r, add_multipoles=False)

(X_ref,Y_ref,pos_ref, overlap_ref) = CircleOfCircles(x_point,y_point,large_circle_r,circle_r,num_samples,1)
(By1_ref, Bx1_ref) = nPoleComponent(N,X_ref,Y_ref,amplitude,offsetAngle,large_circle_r, add_multipoles=False)

 #Plotting the magnetic field and our circles along with their origin
fig, ax = plt.subplots()
ax.use_sticky_edges = False
ax.margins(0.07)
ax.axis('on')
ax.tick_params(direction = 'in',bottom=True,top=True,left=True,right=True)
p = ax.quiver(x_mesh,y_mesh,Bx_whole,By_whole, units = 'xy', cmap = plt.cm.winter,zorder=2,
        width=0.007, headwidth=3.,scale=scl ,headlength=4.5,color='grey')
q = ax.quiver(X,Y,Bx1,By1, units = 'xy', cmap = plt.cm.winter,zorder=2,
        width=0.007, headwidth=5., scale=scl ,headlength=5.5,color='red')
plt.plot(np.imag(pos),np.real(pos),'o', color='red')
plt.plot(X,Y, '.', color='black')
print(overlap1)
plt.show()




#Doing the calculations on the multipoles
t_ref = (B_r(X_ref, Y_ref , Bx1_ref, By1_ref))
sp = np.fft.fft(t_ref)

t = (B_r(X,Y,Bx1, By1))
C = MatrixC(t,number_circles)
M = MatrixM(num_samples,15,large_circle_r,circle_r,pos)




Cp,res,rank,s = np.linalg.lstsq(M,C,rcond=None)


#Plotting the Fourier transform
fig, axs = plt.subplots(2,2)


axs[0,0].plot(np.linspace(0,2*np.pi,len(sp)),np.fft.ifft(sp))
axs[0,0].set_title('Curve from ref vec')

axs[0,1].plot(np.linspace(0,2*np.pi,len(Cp)),np.fft.ifft(Cp))
axs[0,1].set_title('Reconstructed curve')


sp = sp[0:15] #Only take multipoles from main component and following
#sp = (1e4/sp[0])*sp[1:15] #Scale the multipoles
Cp_norm = Cp[0:15] #Only take multipoles from main component and following
#Cp_norm = (1e4/Cp[0])*Cp[1:15] #Scale the multipoles
```

```python
axs[1,0].stem(np.linspace(1,15,15), np.abs((sp[0:15])),  linefmt='C0-',
        markerfmt="␣", basefmt="-b")
axs[1,0].set_title('Ref')


axs[1,1].stem(np.linspace(1,15,15), np.abs((Cp_norm[0:15])), linefmt='C1-',
        markerfmt="␣", basefmt="-")
axs[1,1].set_title('Reconstructed␣multipoles')



np.set_printoptions(precision=3, suppress=True)
plt.show()
```